Nanoscale Advances

ROYAL SOCIETY OF CHEMISTRY

PAPER

View Article Online
View Journal | View Issue

Cite this: *Nanoscale Adv.*, 2025, **7**, 3701

Magnetically recoverable Fe_3O_4@chitosan@Ni_2B: a bio-based catalyst for one-pot green and efficient synthesis of tetrahydrobenzo[*b*]pyrans†

Bashir Mashhourzad and Behzad Zeynizadeh *

Received 7th December 2024
Accepted 23rd April 2025

DOI: 10.1039/d4na01020e

rsc.li/nanoscale-advances

This study investigates the development of a novel and environmentally friendly catalyst, Fe_3O_4@chitosan@Ni_2B nanocomposite, for multicomponent reactions (MCRs). Chitosan (CS), a biopolymer, is used because it is biocompatible, abundant, and has functional groups that can be complexed with metals. Nickel boride (Ni_2B) is used in hydrogenation reactions due to its catalytic properties. The magnetic properties of Fe_3O_4 nanoparticles enable easy separation. Herein, we describe the successful synthesis of the Fe_3O_4@CS@Ni_2B nanocomposite and its use in MCRs for the green synthesis of tetrahydrobenzo[*b*]pyran derivatives. These heterocyclic compounds impress with their diverse biological activities. The research has several advantages, including the implementation of environmentally friendly catalyst protocols, the simplification and cost-effectiveness of the synthesis process, the use of an easily accessible biopolymer, the successful performance of efficient one-pot reactions without additional waste generation, and the easy recycling of the catalyst. This research demonstrates the potential of Fe_3O_4@CS@Ni_2B as a promising catalyst for sustainable and selective MCRs.

1 Introduction

Nowadays, green chemistry has gained significant importance in chemical reactions. Therefore, synthesizing safe chemical compounds and using low-risk materials are becoming essential topics in chemical investigation and industry. The use of catalysis to perform eco-friendly chemical reactions has received much attention in recent years.[1,2] Catalysis is undoubtedly one of the most important components of modern synthetic chemistry, its importance cannot be ignored, and it is also one of the most fundamental foundations of green chemistry.[3] To this end, a good catalyst should have distinctive features, including low manufacturing cost, non-toxicity, high activity, high stability, easy and efficient recovery, high recyclability, biocompatibility, and an environmentally friendly synthesis route.[4] Therefore, the synthesis of safe chemical products based on biopolymers is a crucial topic in the field of catalysts. Chitosan (CS) is a compound that exhibits many of the features mentioned above. CS is a linear amino copolymer composed of β-(1–4)-linked glucosamine units derived from the deacetylation of chitin and is one of the most abundant biopolymers on Earth.[5] This unique biopolymer is composed of various functional groups, such as primary amines, hydroxyl, as well as ethers and acetamides, making CS an exceptional compound to be used in applications such as for dye removal,[6,7] as an adsorbent for metals,[8–12] as a corrosion inhibitor,[13] in wound healing,[14] in drug and gene delivery,[15] as a biological agent,[16,17] and as a catalyst.[18,19] It has also been identified as a versatile biopolymer, an antibacterial, and a harmless, environmentally friendly, and biodegradable material used in a range of agricultural, food, and biopharmaceutical catalyst applications.[20] CS contains a variety of amino groups and hydroxyl groups that can coordinate with metal ions. On the other hand, the complexation reaction is the main reaction of polysaccharides in which the metal can be chelated by complex formation with amino and hydroxyl groups. Hence, it is an excellent material for developing novel green catalytic systems.[21] There are typically three types of catalysts: heterogeneous, homogeneous, and enzyme, each with its advantages and disadvantages, and heterogeneous catalysts are of crucial importance in industry and research. These catalysts have more stable storage conditions and can be separated from the reaction mixture very easily, which causes less waste and pollution and is therefore environmentally friendly.[22,23] The combination of CS and magnetite (Fe_3O_4) is widely used as the catalyst. Magnetic nanoparticles can treat large amounts of wastewater in a short time and can be conveniently separated from the wastewater. In addition to enhancing the separation process, the combination of CS with magnetic nanoparticles can expand the ability of CS by increasing its surface area.[24] Many studies have been conducted on CS and various metals as a catalyst. For example, CS and Pd NPs have been used for the Mizoroki–Heck reaction[18] and magnetic CS Cu(II) for the synthesis of various

Faculty of Chemistry, Urmia University, Urmia 5756151818, Iran. E-mail: bzeynizadeh@gmail.com

† Electronic supplementary information (ESI) available. See DOI: https://doi.org/10.1039/d4na01020e

tetrazoles[25] and magnetic CS nickel(II) for the synthesis of one-pot multicomponent reactions.[26] But, to date, no combination of CS and metal borides has been reported. Metal borides, especially nickel borides, are interesting compounds with unique properties such as superconductivity,[27] high hardness,[28] high melting temperature,[29] high thermal conductivity,[30] and chemical inertness.[31,32] In the early 1950s, Schlesinger and co-workers reported that the reduction of nickel salts with sodium borohydride in aqueous solution produces a black granular material called nickel boride (Ni_2B).[33] Also, Brown *et al.* reported two types of nickel boride. When the borohydride reduction is carried out in an aqueous solution, the product is referred to as a P-1 nickel boride,[34] which is at least as active as RANEY® nickel for double-bond hydrogenation. When the reduction is performed in 95% ethanol, the product is referred to as P-2 nickel boride,[35] which is more sensitive to the double bond structure. Also, the P-1.5 Ni catalyst is prepared in an identical manner using a 50% ethanol–water solution as the solvent.[36] Nickel borides have been widely used as electrodes for oxygen evolution reactions (OERs),[37,38] supercapacitors,[39] adsorbents,[40] desulfurization reactions,[41] and coupling reactions[42,43] and have been shown to be very active catalysts in the hydrogenation of many functional groups.[36,44–46]

Multicomponent reactions (MCRs) have recently been considered the most effective technique in the synthesis of organic compounds and drugs because they generate carbon–carbon and carbon–heteroatom bonds in one pot. Because of their performance and efficacy, MCRs offer a dominant platform to access a sustainable, complication-free, and diversity-oriented synthesis of heterocyclic compounds from simple and cheap starting materials. In addition, MCRs offer some advantages in terms of simplicity and the production of the end product without by-products.[47–50] Many studies have been conducted based on the catalytic properties of CS in one-pot reactions,[51–56] such as the green synthesis of 2-amino-4*H*-chromene derivatives with magnetic CS (Fe_3O_4@CS),[54] the synthesis of spirolactone derivatives using magnetic CS anchored Schiff base nickel(II) complex (Fe_3O_4@CS-SB-Ni^{II})[55] and the synthesis of xanthene derivatives with Fe_3O_4/CS-Ag NPs.[56] In the last few years, tetrahydrobenzo[*b*]pyrans have been the best category of heterocyclic compounds that have attracted great attention as they are components of various heterocyclic natural products and drugs with anti-HIV,[57] antitumor, anticancer[58,59] antibacterial,[60] antitubercular,[61] and antimicrobial[62] properties. Fig. 1 shows a series of synthesized 2-amino-3-cyano-substituted tetrahydrobenzo[*b*]pyrans with intriguing biological efficacies.

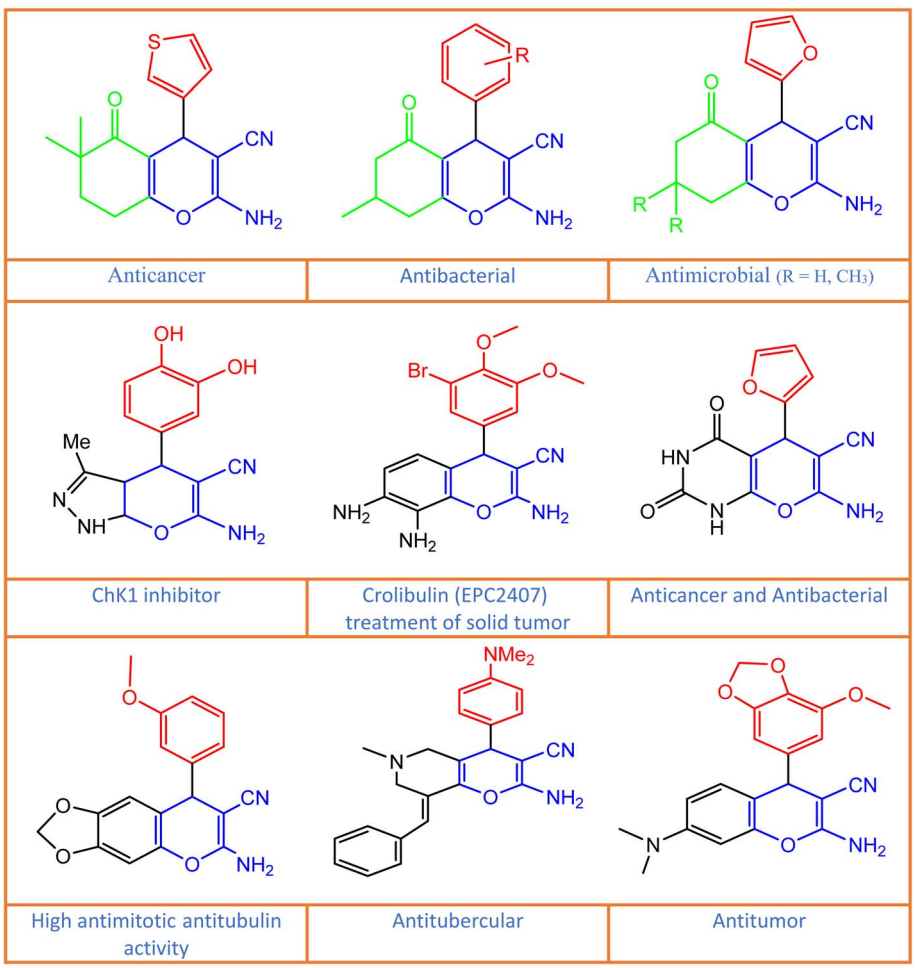

Fig. 1 Bioactivity of synthetic 2-amino-3-cyano-substituted tetrahydrobenzo[*b*]pyran.

Table 1 Comparison of the Fe_3O_4@CS@Ni_2B nanocomposite with some reported catalysts for the synthesis of tetrahydrobenzo[*b*]pyrans

Entry	Catalyst composition	Preparation complexity	Eco-friendly (catalyst preparation)	Eco-friendly (reaction)	Cost material	Reaction time (min)	Yield	Ref.
1	AuNPs@RGO-SH H_2O, reflux	Moderate–complex	No	Yes	High	60	85	63
2	$H_5PW_6Mo_4V_2O_{40}$ H_2O, reflux	Moderate	No	Yes	Moderate	15	95	64
3	SO_4^{2-}/MCM-41 EtOH, reflux	Moderate–complex	No	Yes	Moderate	60	80	65
4	Fe_3O_4@SiO_2@KCC-MPTMS@Cu^{II} Solvent-free, 110 °C	Complex	No	Yes	High	60	96	66
5	GO-ANSA EtOH, reflux	Moderate	No	Yes	Moderate	30	89	67
6	GO–Si–NH_2–PMo Solvent-free, 90 °C	Moderate–complex	No	Yes	Moderate	5	94	68
7	Hal-Py-IL EtOH, 50 °C	Simple	No	Yes	Cheap	120	100	69
8	FNASiPPEA EtOH, 50 °C	Moderate	No	Yes	Cheap	25	92	70
9	[SiO_2^-Caff.]HSO_4 Solvent-free, 100 °C	Simple	No	Yes	Cheap	20	90	71
10	rGO@Fe_3O_4@$ZrCp_2Cl_2$ PEG-400, 100 °C	Moderate–complex	No	Yes	Moderate	60	95	72
11	Fe_3O_4@chitosan@Ni_2B H_2O/EtOH, reflux	Simple	Yes	Yes	Cheap	25	95	This work

In recent years, the development of multicomponent reactions (MCRs) has increasingly been geared towards green reactions. Our work introduces a novel bio-based Fe_3O_4@chitosan@Ni_2B nanocomposite, prepared *via* a simple, low-cost, and environmentally benign route using water/ethanol under reflux. This catalyst not only operates under green reaction conditions but also achieves remarkable performance, delivering yields of up to 95% within approximately 25 min. A thorough comparison with ten reported catalysts highlights several key advantages of our system in terms of synthesis simplicity, reaction efficiency, and overall cost-effectiveness (Table 1).

For instance, gold nanoparticles supported on thiol-functionalised reduced graphene oxide (AuNPs@RGO-SH), while effective and green during the catalytic reaction, require the use of expensive gold and involve complex surface modifications that complicate their synthesis.[63] In contrast, our catalyst utilises chitosan, a naturally abundant and biodegradable polymer, thereby reducing costs and streamlining the synthetic process. Similarly, the quaternary vanado-molybdotungstophosphoric acid ($H_5PW_6Mo_4V_2O_{40}$) catalyst anchored on natural montmorillonite operates in an eco-friendly medium; however, its multistep preparation, which employs harsh reagents and conditions, detracts from its economic and environmental viability.[64]

Likewise, catalysts such as sulfated MCM-41 nanoparticles (SO_4^{2-}/MCM-41) have demonstrated efficiency under green conditions but necessitate the use of hazardous chemicals and prolonged synthesis times.[65] The Fe_3O_4@SiO_2@KCC-1@MPTMS@Cu^{II} catalyst, although highly active in a solvent-free, green environment, suffers from a labour-intensive and costly multi-stage preparation.[66] Furthermore, catalysts based on functionalised graphene oxide modified with either 4-amino-3-hydroxy-1-naphthalenesulfonic acid (GO-ANSA)[67] or through the graphene oxide functionalized organic–inorganic hybrid (GO–Si–NH_2–PMo)[68] demand elaborate synthetic procedures and often non-green solvents during their preparation despite operating under environmentally benign reaction conditions.

Other systems, such as halloysite nanoclay combined with a sulfonic acid-based ionic liquid (Hal-Py-IL), are derived from natural materials and utilised in green media; yet, their reaction kinetics are slower than those of our nanocomposite.[69] Similarly, the Fe_3O_4@nano-almond-shell catalyst modified with $Si(CH_2)_3$/2-(1-piperazinyl)ethylamine (FNASiPPEA),[70] although based on renewable supports, requires additional modification steps that extend the overall reaction time. The caffeine-supported silica catalyst ([SiO_2^-Caff.]HSO_4),[71] while offering a bio-based approach, shows lower catalytic efficiency and slower reaction rates in comparison. Lastly, the immobilised zirconocene chloride on a magnetite-reduced graphene oxide catalyst (rGO@Fe_3O_4@$ZrCp_2Cl_2$),[72] though innovative and green during the reaction, is hampered by a complicated synthesis route and higher reagent costs.

Notably, all of these catalytic systems operate under environmentally friendly reaction conditions. However, our catalyst is particularly noteworthy because, beyond its green reaction conditions, it is also straightforward and eco-friendly to synthesize, offers faster reaction kinetics, allows for easy magnetic separation, and provides a high yield. Given these

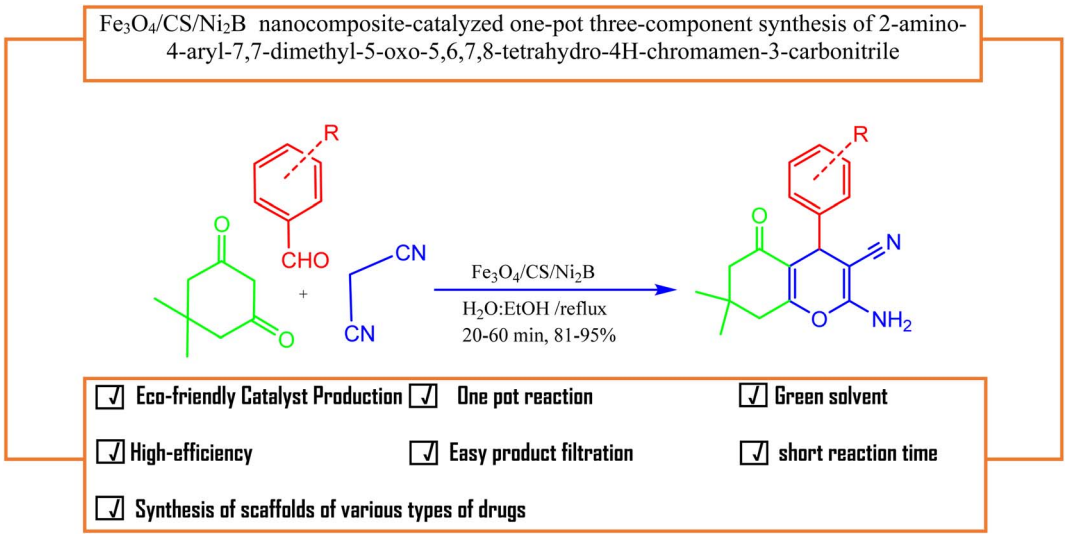

Scheme 1 Fe_3O_4@CS@Ni_2B nanocomposite-catalyzed one-pot three-component synthesis of 2-amino-4-aryl-7,7-dimethyl-5-oxo-5,6,7,8-tetrahydro-4*H*-chromamen-3-carbonitrile.

advantages, we have designed a novel, efficient, and sustainable catalytic system, Fe_3O_4@CS@Ni_2B (and CS@Ni_2B), to improve the green synthesis of 2-amino-7,7-dimethyl-5-oxo-4-aryl-5,6,7,8-tetrahydro-4*H*-chromene-3-carbonitrile. Considering the remarkable benefits of multicomponent reactions (MCRs), this study presents the synthesis of chromene derivatives (**3a–o**)

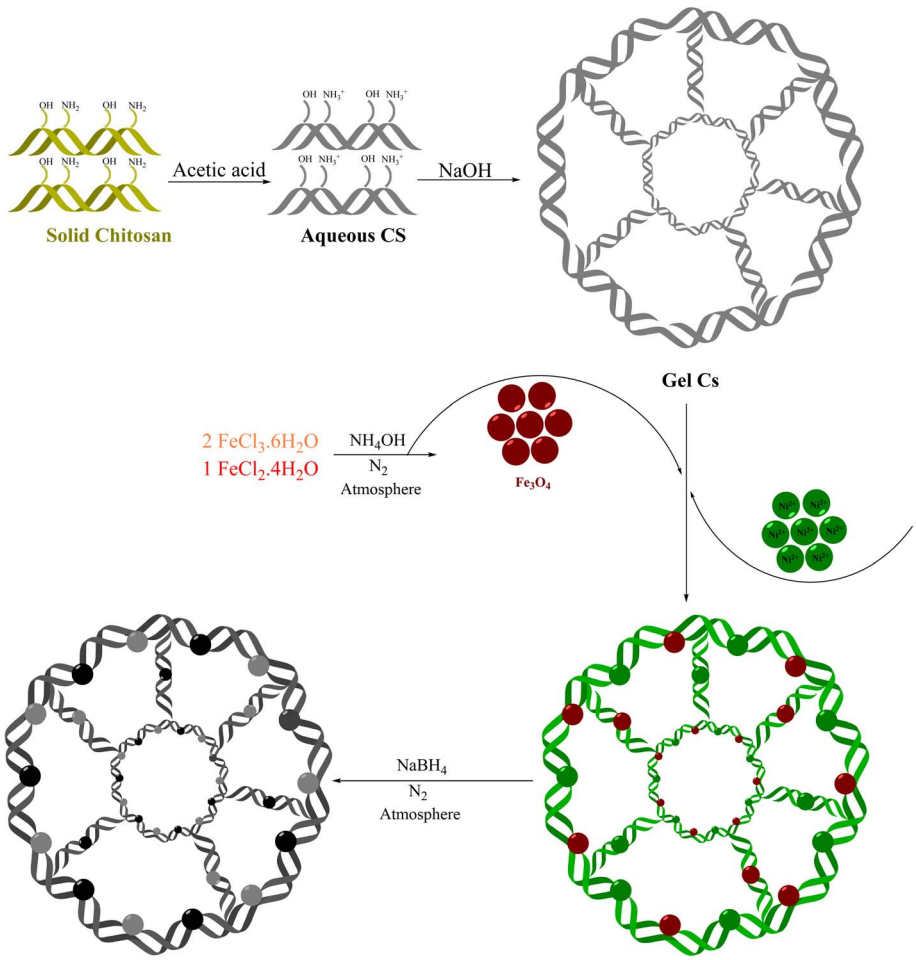

Scheme 2 Schematic illustration of the preparation of the Fe_3O_4@CS@Ni_2B nanocomposite.

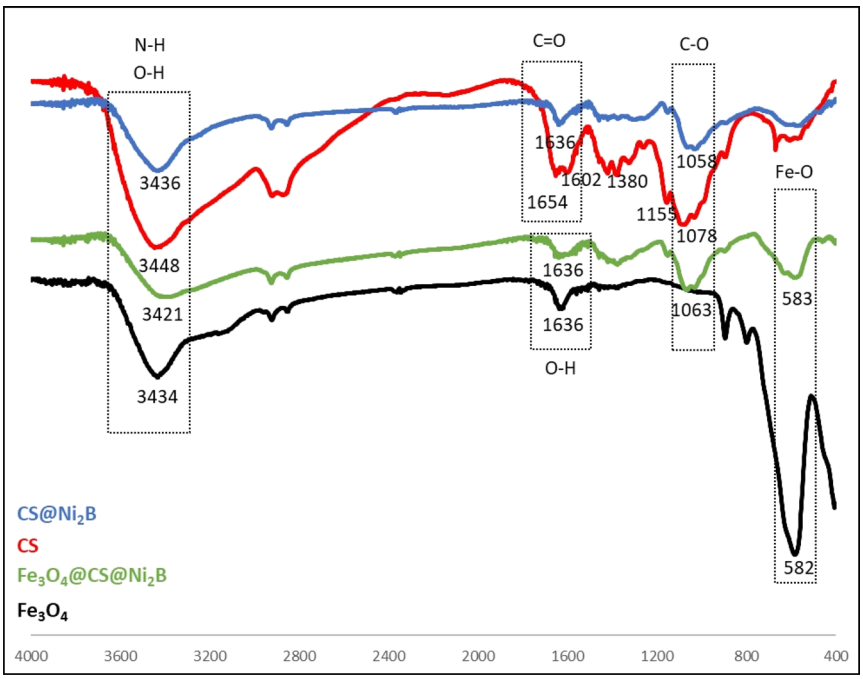

Fig. 2 FT-IR spectra of Fe_3O_4, CS, CS@Ni_2B, and Fe_3O_4@CS@Ni_2B nanocomposites.

through a three-component reaction involving dimedone, malononitrile, and aromatic aldehydes *via* a one-pot condensation process (Scheme 1).

2 Results and discussion

2.1 Catalyst synthesis and characterization

Our research on the benefits of green, recyclable, and innovative heterogeneous catalysts in organic transformations led us to developing a novel heterogeneous catalyst (Fe_3O_4@CS@Ni_2B) for the environmentally friendly synthesis of tetrahydrobenzo[*b*]pyran. The nanocatalyst was synthesized as outlined in Scheme 2. Initially, the chitosan gel (CS) was prepared, and then nickel(II) ions were incorporated.

Following that, magnetite nanoparticles (Fe_3O_4), which had already been synthesized using the chemical co-precipitation method, were added to this composite, and finally nickel boride was produced from sodium borohydride by the reduction process.

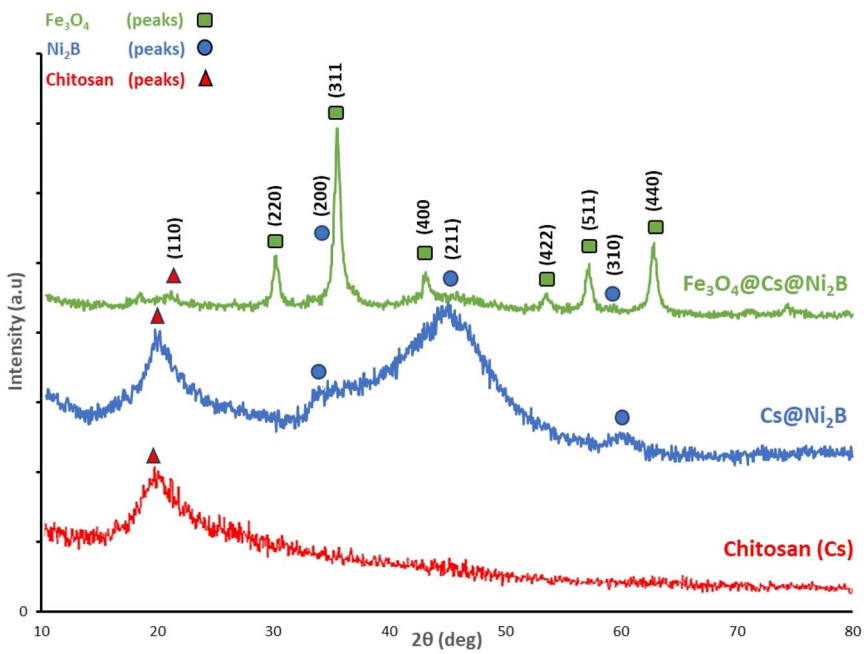

Fig. 3 XRD patterns of chitosan (CS), and CS@Ni_2B and Fe_3O_4@CS@Ni_2B nanocomposites.

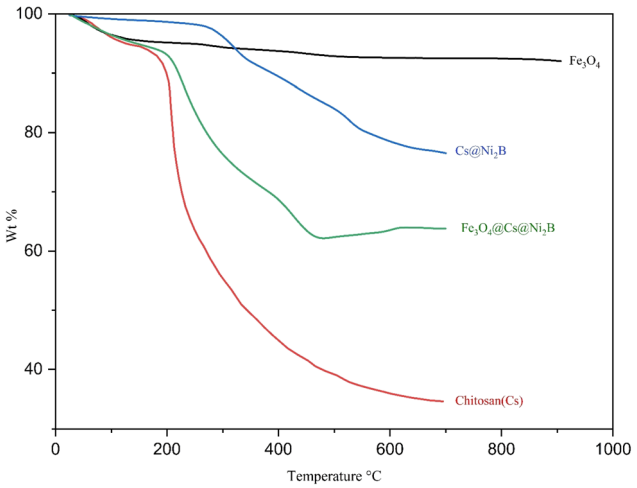

Fig. 4 TGA diagrams of chitosan (CS), Fe_3O_4, CS@Ni_2B, and Fe_3O_4@CS@Ni_2B.

2.2 Characterization of the Fe_3O_4@CS@Ni_2B nanocomposite

The thus-synthesized nanocomposite was fully characterized using various analytical techniques, such as FT-IR, FESEM, EDX, ICP, VSM, XRD, TGA, and BET analyses.

2.2.1 FT-IR analysis. The FT-IR spectra of Fe_3O_4 nanoparticles, CS, CS@Ni_2B, and Fe_3O_4@CS@Ni_2B are shown in Fig. 2. The FT-IR spectra of the Fe_3O_4 NPs were verified by the characteristic absorption peak of the Fe–O bond at around 582 cm^{-1}, confirming the accurate synthesis of iron oxide nanoparticles. The absorption peaks at approximately 3433 cm^{-1} and 1636 cm^{-1} correspond to the stretching and bending vibrations, respectively, of the O–H bond on the surface of the Fe_3O_4 magnetic nanoparticles.[73]

The IR spectrum of CS shows main absorption bands at 3448 cm^{-1} (O–H and N–H stretch), 1654 cm^{-1} (stretching of the C=O amide group) 1602 cm^{-1} (angular deformation of the N–H bonds of the amino groups), 1380 cm^{-1} (symmetric angular deformation of CH_3), 1155 cm^{-1} (asymmetric bridge–O–stretch) and 1078 cm^{-1} (skeletal vibration involving the C–O stretch).[74]

2.2.2 XRD analysis. Fig. 3 shows the XRD patterns of CS, CS@Ni_2B, and Fe_3O_4@CS@Ni_2B. The diagram clearly shows that the broad peaks at $2\theta = 20°$ and $2\theta = 45°$ correspond to the (110) crystallographic planes of CS and the (211) tetragonal planes of Ni_2B (JCPDS 00-048-1222), respectively. However, only broad peaks at 20° corresponding to CS and other peaks at 35°, 45°, and 60° corresponding to amorphous Ni_2B are identified in the XRD patterns of the CS@Ni_2B catalyst (JCPDS 00-025-0576).[39,75,76]

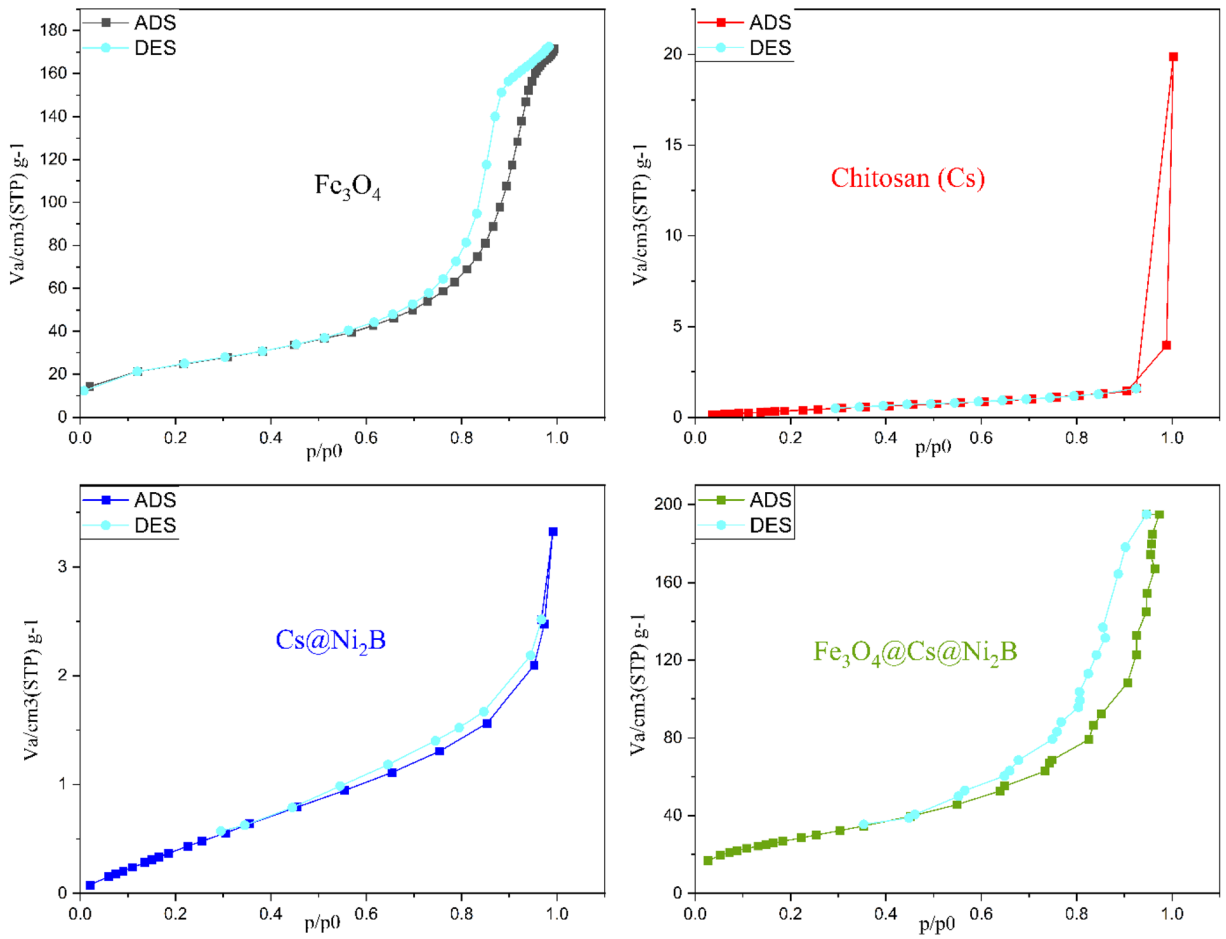

Fig. 5 N_2 adsorption–desorption isotherms of Fe_3O_4, chitosan (CS), CS/Ni_2B and Fe_3O_4/CS/Ni_2B.

Table 2 Results of BET analysis for chitosan (CS), Fe_3O_4, and CS@Ni_2B and Fe_3O_4@CS@Ni_2B nanocomposite systems[a]

Sample	BET surface area (S_{BET}) ($m^2\ g^{-1}$)	V_m (cm^3(STP) g^{-1})	Pore volume (V_p) ($cm^3\ g^{-1}$)	Pore size (nm)
Chitosan (CS)	1.9872	0.4566	0.009	18.55
Fe_3O_4	86.55	19.8874	0.26	12.048
CS@Ni_2B	2.13	0.4903	0.005	9.49
Fe_3O_4@CS@Ni_2B	101.02	23.21	0.3016	11.94

[a] S_{BET}: Brunauer–Emmett–Teller surface area. V_m: Brunauer–Emmett–Teller volume of monolayer coverage. V_p: BJH desorption cumulative volume of pores.

For Fe_3O_4@chitosan@Ni_2B, one peak at 2θ around 20° corresponding to CS, three peaks at 35°, 45°, and 60° corresponding to amorphous Ni_2B and six diffraction peaks at 2θ around 30.3°, 35.5°, 43.1°, 53.5°, 57.1°, and 62.8° correspond to the (220), (311), (400), (422), (511), and (440) planes, respectively (JCPDS 00-001-1111). These are standard patterns of the inverse cubic spinel magnetite (Fe_3O_4) crystal structure, indicating the formation of magnetite in the desired composition.

2.2.3 Thermal gravimetric analysis (TGA). In this study, thermogravimetric analysis (TGA) was conducted in an N_2 atmosphere over a temperature range of 0–700 °C to evaluate the thermal stability and decomposition behavior of the synthesized nanocomposite system. To ensure a comprehensive understanding of the thermal properties at each fabrication step, TGA was performed separately for Fe_3O_4 nanoparticles, chitosan (CS), CS@Ni_2B, and Fe_3O_4@CS@Ni_2B composite (Fig. 4).

A typical TGA curve of Fe_3O_4 shows a minor weight loss (1–3%) below 200 °C, attributed to physisorbed water and volatile impurities. Between 200 and 600 °C, the curve remains stable, reflecting Fe_3O_4's high thermal stability in an inert atmosphere. Above 600 °C, a gradual or stepwise weight loss (5–10% up to 900 °C) may occur, influenced by factors like purity, particle size, and the synthesis method.

The TGA curve of chitosan reveals distinct degradation stages. An initial 5–10% weight loss at 25–100 °C is due to

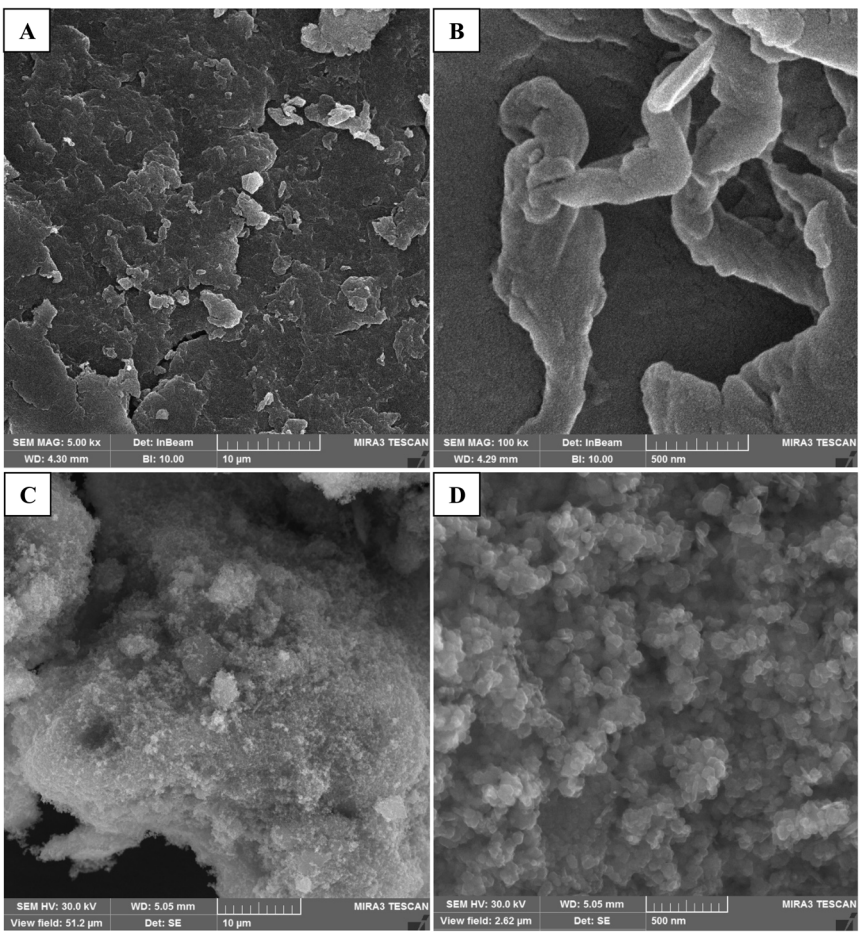

Fig. 6 FESEM images of chitosan (A and B) and Fe_3O_4 (C and D).

moisture and residual solvent evaporation. Between 100 and 300 °C, a major 50–60% loss occurs from glycosidic bond cleavage and deacetylation, releasing volatile byproducts (CO_2, NH_3, and hydrocarbons). A slower 10–15% loss from 300 to 400 °C indicates continued degradation and partial carbonization, leading to char formation. Beyond 400 °C, the curve stabilizes, leaving a 20–30% residue of thermally stable carbonized products.

The TGA curve for the CS@Ni_2B composite reveals distinct thermal behavior compared to pure chitosan. Below 150 °C, the TGA curve shows minor weight loss due to moisture evaporation and residual solvents. While nickel boride remains thermally stable, its dispersion in chitosan affects moisture retention. Between 200 °C and 400 °C, significant mass loss occurs as glycosidic bonds break, deacetylation takes place, and volatile fragments are released. Nickel boride may alter this process by interacting with –OH and –NH_2 groups, shifting the decomposition onset, and acting as a barrier to slow degradation, thereby enhancing thermal stability. Beyond 400 °C, gradual weight loss leads to carbon-rich char formation, with nickel boride remaining intact, significantly contributing to the final residual mass plateau near 700 °C.

The TGA thermogram clearly shows three stages of mass loss in the Fe_3O_4@CS@Ni_2B nanocomposite at temperatures of 25–200 °C, 200–400 °C, and 400–500 °C. The first stage involves weight loss due to the removal of physisorbed water and the degradation of organic components, such as surface hydroxyl groups, within the range of 25–200 °C. The second stage occurs between 200 °C and 400 °C, where the chitosan polymer structure undergoes degradation. In the final stage, within the temperature range of 400–500 °C, the breakdown of saccharide rings, Ni_2B decomposition, and the thermal decomposition of Fe_3O_4 take place.

2.2.4 BET analysis. The BET analysis and surface area measurements provide valuable insights into how layering affects the catalytic properties of Fe_3O_4, chitosan (CS), CS@Ni_2B, and Fe_3O_4@CS@Ni_2B. Each material exhibits distinct adsorption–desorption isotherms (Fig. 5) and surface characteristics (Table 2), reflecting structural and textural transformations.

Chitosan (CS) has a relatively low BET surface area of 1.9872 $m^2\ g^{-1}$, with no H3 hysteresis in its isotherm, indicating a lack of slit-shaped pores typically associated with layered structures. This suggests that chitosan alone has limited porosity, making it less effective for applications requiring high adsorption capacity. In contrast, Fe_3O_4 shows a significantly higher BET surface area of 86.55 $m^2\ g^{-1}$. Its isotherm reveals H3 hysteresis, characteristic of slit-shaped pores formed by aggregated plate-

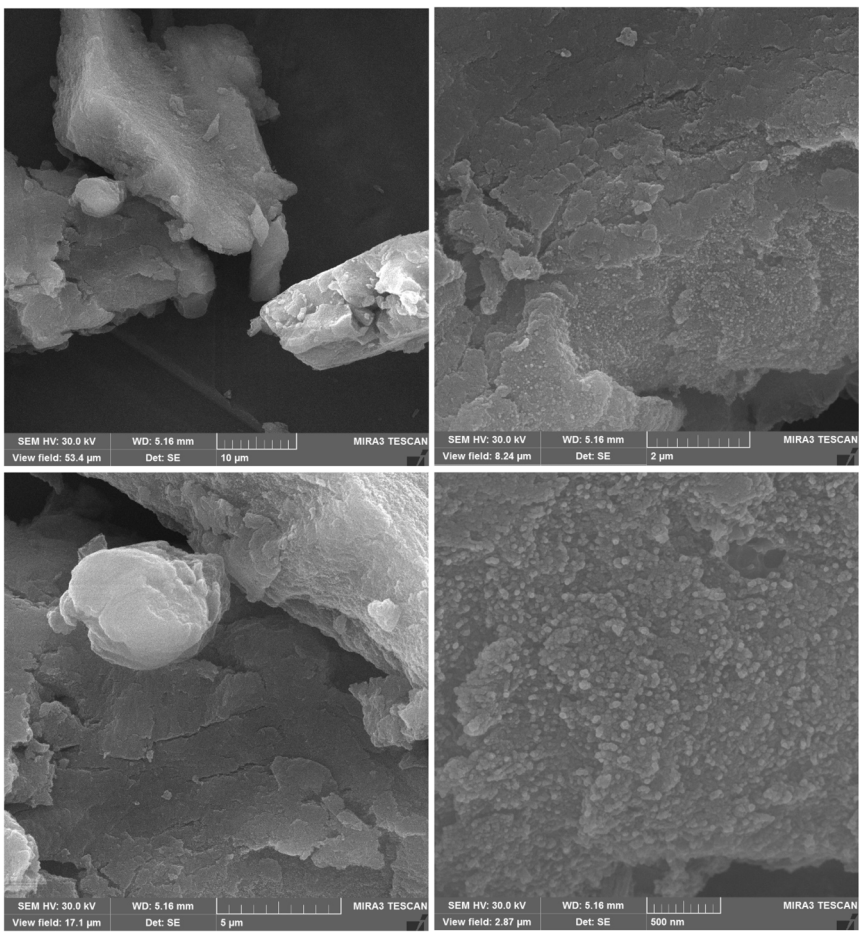

Fig. 7 FESEM image of the CS@Ni_2B nanocomposite.

like particles. This increased porosity enhances Fe_3O_4's adsorption capacity, making it well-suited for catalytic and adsorption applications. When Ni_2B is incorporated into chitosan to form CS@Ni_2B, the BET surface area experiences only a slight increase to 2.13 $m^2\ g^{-1}$. While this indicates that Ni_2B does not drastically change the overall porosity, the presence of H3 hysteresis suggests that it contributes to the formation of slit-shaped pores, likely enhancing adsorption in a limited capacity. The most notable improvement is observed in Fe_3O_4@CS@Ni_2B, which exhibits the highest BET surface area of 101.02 $m^2\ g^{-1}$. The synergistic combination of Fe_3O_4's porous structure with Ni_2B's pore-forming effects significantly enhances the overall surface area and adsorption capacity. The strong H3 hysteresis further confirms the presence of slit-shaped pores, optimizing the material's potential for catalytic and adsorption-based applications.

In summary, the addition of layers plays a critical role in modifying the surface area and porosity. While chitosan alone has minimal adsorption capability, Fe_3O_4 introduces substantial porosity. The CS@Ni_2B composite shows some structural improvements, primarily through the introduction of slit-shaped pores. However, the most significant enhancement occurs with Fe_3O_4@CS@Ni_2B, which achieves the highest surface area and an optimized pore structure. These findings underscore the exceptional catalytic potential of Fe_3O_4@CS@Ni_2B, making it a strong candidate for applications requiring efficient adsorption and catalytic performance.

2.2.5 Field emission scanning electron microscopy (FESEM) analysis. FESEM images of chitosan (Fig. 6A and B) show an interconnected fibrous network with smooth and irregular regions, indicating differences in chain entanglement and hydrogen bonds. The observed microporosity enhances the surface area, supporting adsorption and catalytic applications. The roughness of chitosan facilitates nanoparticle dispersion, ensuring structural stability.

Fe_3O_4 nanoparticles (Fig. 6C and D) exhibit aggregation due to magnetic interactions, forming a porous and granular structure. The presence of voids and channels between clusters enhances mass transport properties, optimizing its role in catalysis and environmental remediation.

The CS@Ni_2B nanocomposite (Fig. 7) presents a layered morphology with Ni_2B nanoparticles distributed within chitosan layers. Hydrogen bonding and electrostatic interactions stabilize the composite, preventing Ni_2B agglomeration and ensuring homogeneous dispersion. Compared to Fe_3O_4@CS@Ni_2B, its smoother surface indicates improved nanoparticle uniformity.

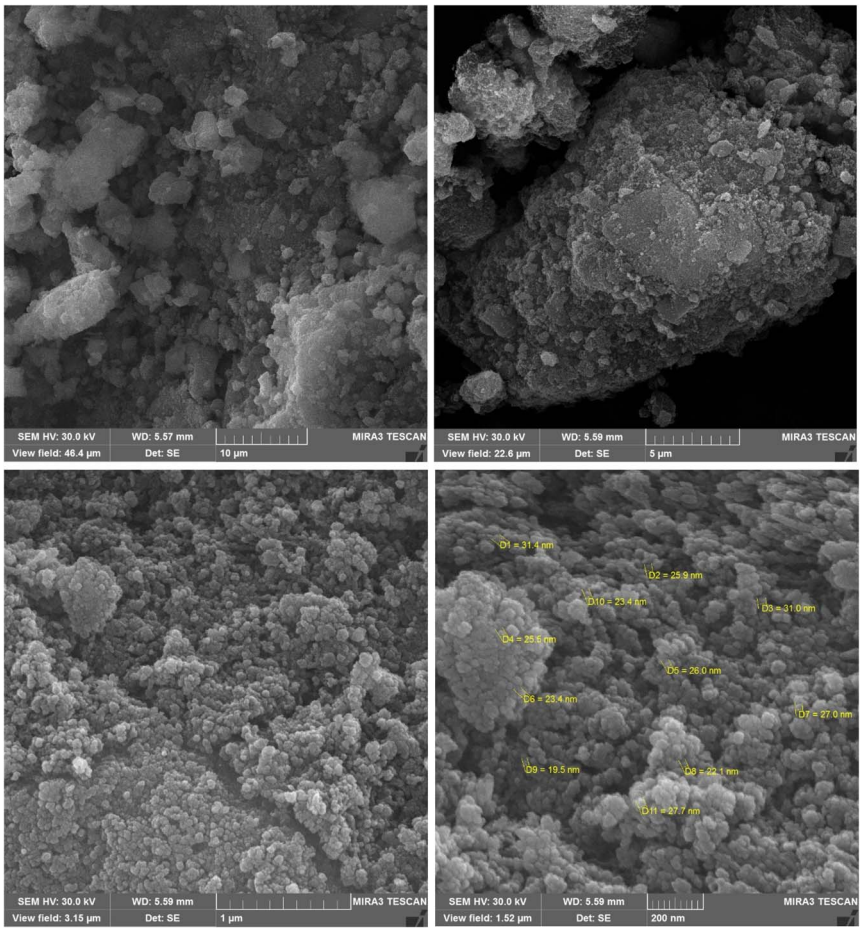

Fig. 8 FESEM image of the Fe_3O_4@CS@Ni_2B nanocomposite.

The Fe_3O_4@CS@Ni_2B composite (Fig. 8) displays a rougher and more porous structure due to Fe_3O_4 incorporation, increasing the distance between chitosan layers. BET analysis confirms significant surface area enhancement (101.02 m^2 g^{-1} for Fe_3O_4@CS@Ni_2B *vs.* 2.13 m^2 g^{-1} for CS@Ni_2B), which facilitates catalytic reactions by improving mass transport and reactant accessibility.

Fe_3O_4@CS@Ni_2B nanoparticles exhibit a size range of 11–31 nm. Compared to CS@Ni_2B, their surface is more irregular and porous due to Fe_3O_4 aggregation. Ni_2B is better dispersed in CS@Ni_2B, whereas Fe_3O_4 alters uniformity in the composite. The incorporation of Fe_3O_4 significantly increases the porosity and surface area, boosting the catalytic performance. Chitosan stabilizes the composite, preventing nanoparticle agglomeration and enhancing dispersion. Fe_3O_4 contributes magnetic properties and additional porosity, while Ni_2B acts as the active catalytic site with high reactivity.

The FESEM study reveals the morphological evolution of the Fe_3O_4@CS@Ni_2B nanocomposite, showing its superior porosity, surface area, and catalytic potential. These findings provide critical insights for optimizing the synthesis and enhancing functional applications in catalysis and environmental remediation.

EDX maps of CS@Ni_2B (Fig. 9) show the structure and composition of the CS@Ni_2B composite.

EDX maps show that boron is distributed in localized clusters, indicating the nucleation sites for Ni_2B.

Nitrogen is uniformly spread, confirming the consistent presence of the chitosan matrix throughout the composite. Nickel appears in high-intensity regions overlapping with boron, verifying the formation of the Ni_2B phase.

The uniform nitrogen distribution, along with the localized boron and nickel clusters, suggests a successful *in situ* synthesis that integrates the inorganic phase within the organic matrix. This structure not only stabilizes Ni_2B but may also enhance interfacial interactions, improving catalytic or adsorptive properties. The Fe_3O_4@CS@Ni_2B nanocomposite, analyzed through EDX elemental mapping (Fig. 10), reveals a well-integrated hybrid material with distinct structural and functional characteristics. The SEM image shows a heterogeneous and porous morphology, where the inorganic phases (Fe_3O_4 and Ni_2B) are embedded within the organic chitosan matrix. This rough texture increases the surface area and catalytic efficiency.

The EDX maps provide deeper insights into elemental distribution. Boron appears in localized high-intensity regions, confirming selective nucleation of Ni_2B, which is essential for catalytic activity. Iron is observed in distinct clusters, representing Fe_3O_4 nanoparticles, which impart magnetic properties, crucial for separation and reusability. Nickel strongly co-localizes with boron, verifying the formation of Ni_2B, while nitrogen is uniformly distributed, demonstrating the continuity of the chitosan matrix, which stabilizes the inorganic phase and provides structural integrity.

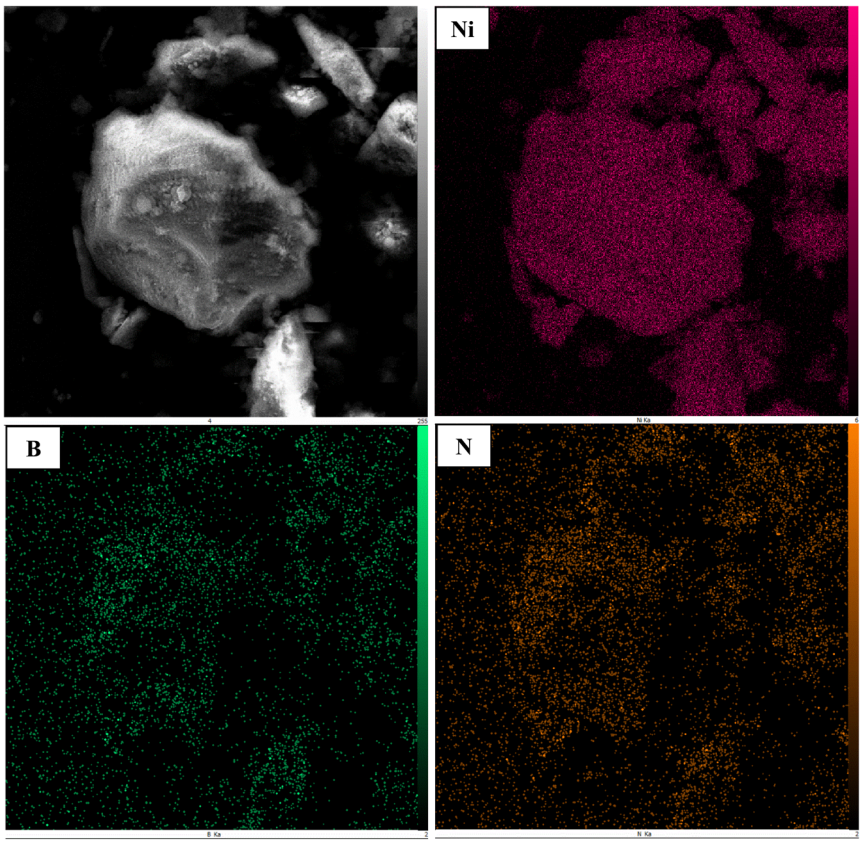

Fig. 9 SEM-based elemental mapping of the as-synthesized CS@Ni_2B nanocomposite.

This composite exhibits a synergistic interplay between its components. The Fe_3O_4 phase introduces magnetic responsiveness, allowing for easy separation, while Ni_2B contributes to catalytic functionality. Chitosan serves as a stabilizing scaffold, preventing agglomeration and enhancing interfacial interactions. These characteristics make the material highly promising for applications in heterogeneous catalysis, magnetically assisted separation, and potentially biomedical fields.

The well-defined elemental domains suggest a controlled *in situ* synthesis, optimizing interfacial contact and functional integration.

2.2.6 VSM analysis. Using a vibrating sample magnetometer (VSM), the magnetic properties of Fe_3O_4@CS@Ni_2B were investigated by applying a magnetic field back and forth in the range of 10 000 to −10 000 Oe. Fig. 11 shows the room-temperature hysteresis loop of Fe_3O_4@CS@Ni_2B. The curve exhibits no coercivity, indicating superparamagnetism, and the magnetization behavior disappears when the applied magnetic field is removed. The Fe_3O_4@CS@Ni_2B nanocomposite demonstrates a magnetic saturation intensity of 20.7 emu g^{-1}, enabling it to be magnetically separated from the reaction mixture.

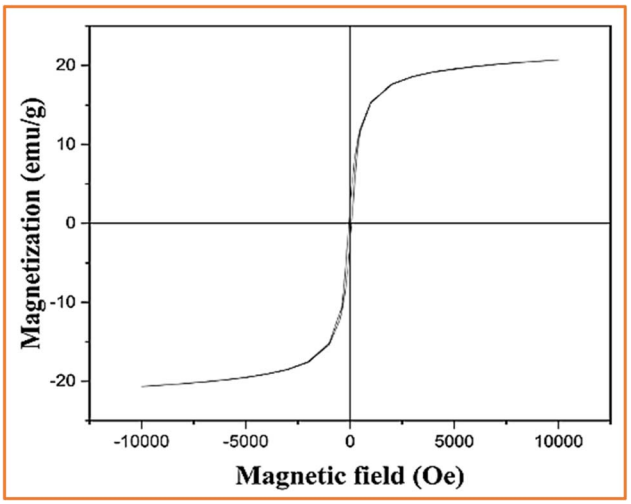

Fig. 11 VSM magnetization diagram of the Fe_3O_4@CS@Ni_2B nanocomposite.

2.3 Evaluation of the catalytic performance of the Fe_3O_4@CS@Ni_2B and CS@Ni_2B nanocatalysts for the synthesis of tetrahydrobenzo[*b*]pyrans

In this research, after characterizing the catalyst for the synthesis of the target products, the efficiency and catalytic activity of the as-prepared Fe_3O_4@CS@Ni_2B and CS@Ni_2B nanocomposites were investigated for the one-pot synthesis of tetrahydrobenzo[*b*]pyran *via* the three-component condensation reaction of dimedone, malononitrile, and aromatic aldehydes. A study was conducted to optimize the reaction conditions for the synthesis of 2-amino-7,7-dimethyl-5-oxo-4-phenyl-5,6,7,8-tetrahydro-4*H*-chromene-3-carbonitrile. This was

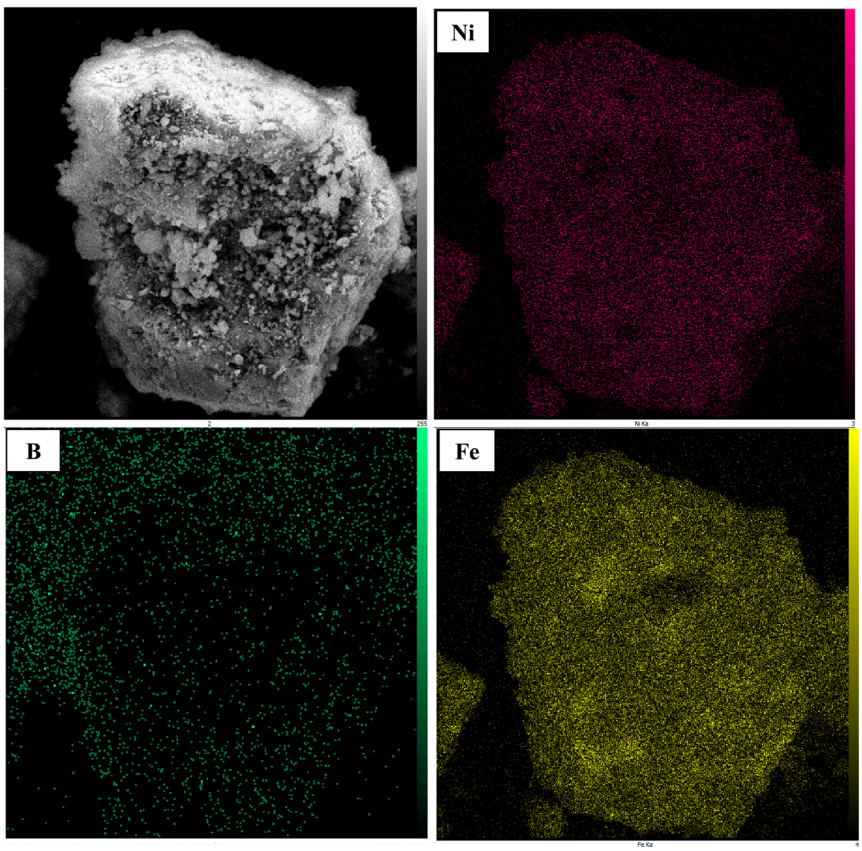

Fig. 10 SEM-based elemental mapping of the as-synthesized Fe_3O_4@CS@Ni_2B nanocomposite.

Table 3 Optimization of the reaction conditions for the one-pot three-component synthesis of 2-amino-7,7-dimethyl-5-oxo-4-phenyl-5,6,7,8-tetrahydro-4*H*-chromene-3-carbonitrile[a]

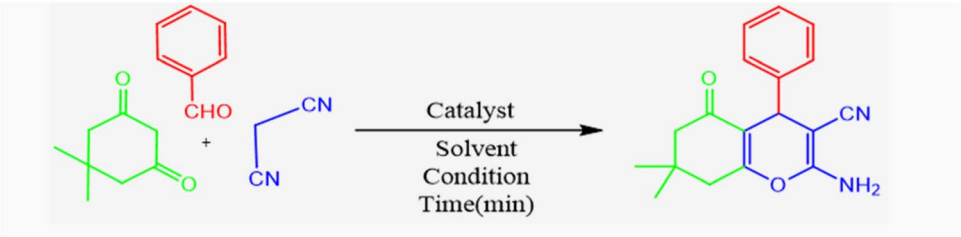

Entry	Catalyst	Catalyst loading (mg)	Solvent	Condition	Time (min)	Yield%	Conversion (%)
1	Fe_3O_4@CS@Ni_2B	30	CH_2Cl_2	Reflux	180	—	—
2	Fe_3O_4@CS@Ni_2B	30	MeOH	Reflux	60	40	50
3	Fe_3O_4@CS@Ni_2B	20	EtOH	Reflux	60	70	75
4	Fe_3O_4@CS@Ni_2B	30	THF	Reflux	90	20	25
5	Fe_3O_4@CS@Ni_2B	30	CH_3CN	Reflux	90	30	40
6	Fe_3O_4@CS@Ni_2B	40	*n*-Hexane	Reflux	120	—	—
7	Fe_3O_4@CS@Ni_2B	30	EtOAc	Reflux	120	—	—
8	Fe_3O_4@CS@Ni_2B	20	H_2O	Reflux	50	82	85
9	Fe_3O_4@CS@Ni_2B	20	H_2O	r.t.	180	25	30
10	Fe_3O_4@CS@Ni_2B	20	H_2O/EtOH (1 : 1)	70 °C	60	65	70
11	**Fe_3O_4@CS@Ni_2B**	**20**	**H_2O/EtOH (1 : 1)**	**Reflux**	**25**	**95**	**96**
12	Fe_3O_4@CS@Ni_2B	30	H_2O/EtOH (1 : 1)	Reflux	25	95	96
13	Fe_3O_4@CS@Ni_2B	20	H_2O/EtOH (1 : 1)	r.t.	180	35	40
14	Fe_3O_4@CS@Ni_2B	15	H_2O/EtOH (1 : 1)	Reflux	60	85	88
15	Fe_3O_4@CS@Ni_2B	30	Solvent-free	110 °C	60	45	55
16	CS@Ni_2B	20	H_2O	Reflux	60	80	85
17	CS@Ni_2B	15	H_2O/EtOH (1 : 1)	Reflux	60	70	75
18	CS@Ni_2B	30	H_2O/EtOH (1 : 1)	Reflux	40	91	92
19	**CS@Ni_2B**	**20**	**H_2O/EtOH (1 : 1)**	**Reflux**	**40**	**91**	**92**

[a] All reactions were carried out with benzaldehyde (1 mmol), dimedone (1 mmol), and malononitrile (1 mmol) in a 4 mL solvent.

achieved through a one-pot, three-component reaction involving dimedone, malononitrile, and benzaldehyde (Table 3). The reaction was carried out using the Fe_3O_4@CS@Ni_2B and CS@Ni_2B nanocomposite systems.

To achieve optimized reaction conditions, experiments were conducted to assess the impact of various solvents, catalyst quantities, and temperatures. To determine the best solvent, a test reaction was performed with 20 to 40 mg of the Fe_3O_4@CS@Ni_2B nanocatalyst in various solvents, including CH_2Cl_2, MeOH, EtOH, THF, CH_3CN, *n*-hexane, EtOAc, H_2O, H_2O/EtOH (1 : 1), and solvent-free conditions. Better performance was achieved when H_2O : EtOH was used as the optimal solvent in a 1 : 1 ratio compared to other solvents studied for this reaction. The model reactions also demonstrated the influence of temperature. The observations showed that reflux conditions yielded the best results. According to the data in Table 3, when the catalyst quantity was increased from 20 to 30 mg, both the product yield and reaction duration remained unchanged. However, reducing the catalyst amount from 20 to 15 mg resulted in a decrease in the product yield and an increase in the reaction duration. Therefore, it was determined that 20 mg is the optimal nanocatalyst loading (Table 3, entry 11). The same conditions were applied to the CS@Ni_2B catalyst, and the results are shown in Table 3. According to the data, the solvent, temperature, and catalyst amount were the same as for Fe_3O_4@CS@Ni_2B. Notably, the Fe_3O_4@CS@Ni_2B catalysts exhibited superior efficiency and faster reaction times. After optimizing the reaction conditions, a protocol for the one-pot synthesis of tetrahydrobenzo[*b*]pyran scaffolds was developed to demonstrate the application efficiency of the new magnetic nanocomposite in organic synthesis. As shown in Table 4, under the optimized reaction conditions, various electron-donating and electron-withdrawing benzaldehydes were examined while keeping malononitrile and dimedone constant for the synthesis of a range of corresponding tetrahydrobenzo[*b*]pyrans. All substituted aromatic aldehydes successfully produced the desired products in good to excellent yields (81–95%).

Furthermore, the basic amino sites precisely determined the reaction process for tetrahydrobenzo[*b*]pyran derivatives in the presence of the Fe_3O_4@CS@Ni_2B catalyst using a three-component coupling strategy. It is believed that the reaction begins with the Knoevenagel condensation of malononitrile (**2**) and aromatic aldehyde (**3a–o**) to produce arylidene malononitrile (**A**). In the second step, dimedone undergoes Michael addition to arylidene malononitrile to generate an intermediate

Table 4 One-pot synthesis of tetrahydrobenzo[*b*]pyrans in the presence of Fe_3O_4@CS@Ni_2B nanocomposite[a]

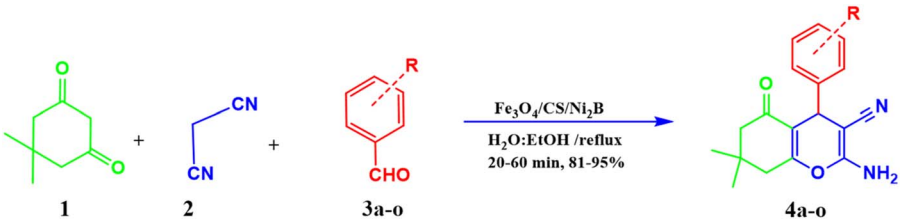

1 2 3a-o 4a-o

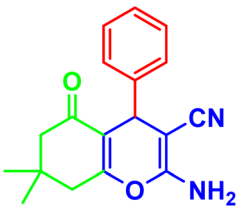

4a
$T = 25$ min, $Y = 95\%$, $C = 96\%$

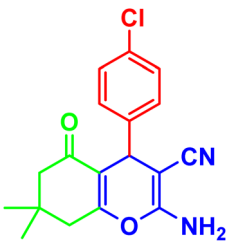

4b
$T = 20$ min, $Y = 93\%$, $C = 94\%$

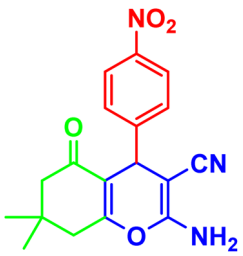

4c
$T = 30$ min, $Y = 92\%$, $C = 96\%$

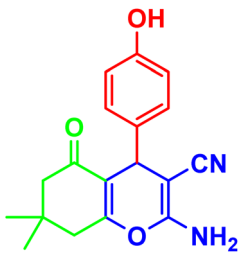

4d
$T = 40$ min, $Y = 90\%$, $C = 91\%$

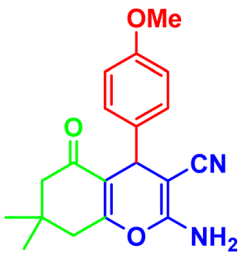

4e
$T = 30$ min, $Y = 90\%$, $C = 94\%$

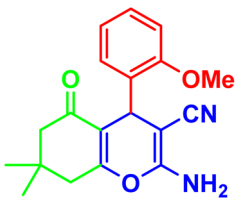

4f
$T = 35$ min, $Y = 90\%$, $C = 91\%$

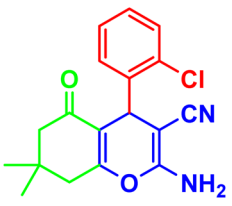

4g
$T = 30$ min, $Y = 90\%$, $C = 94\%$

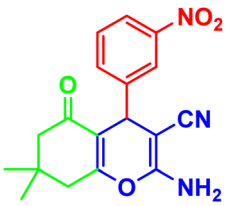

4h
$T = 40$ min, $Y = 83\%$, $C = 92\%$

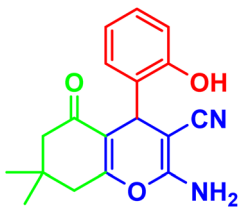

4i
$T = 45$ min, $Y = 85\%$, $C = 88\%$

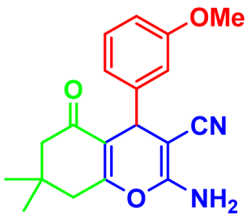

4j
$T = 30$ min, $Y = 90\%$, $C = 93\%$

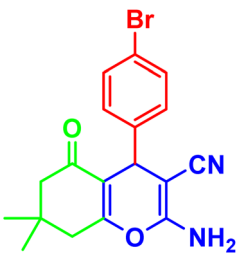

4k
$T = 30$ min, $Y = 93\%$, $C = 95\%$

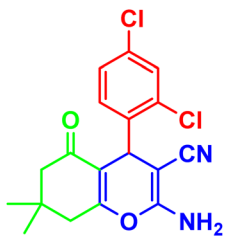

4l
$T = 25$ min, $Y = 90\%$, $C = 92\%$

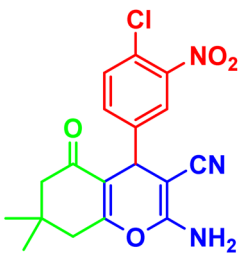

4m
$T = 30$ min, $Y = 90\%$, $C = 97\%$

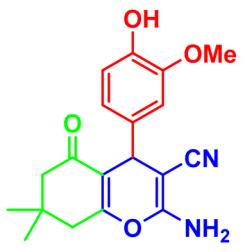

4n
$T = 50$ min, $Y = 81\%$, $C = 88\%$

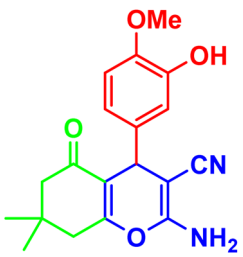

4o
$T = 60$ min, $Y = 85\%$, $C = 93\%$

[a] All reactions were carried out in 5 mL of solvent H_2O/EtOH (1 : 1); Y = yield; T = time; C = conversion.

(**B**). Finally, intramolecular cyclization occurs (**C**), followed by protonation of the intermediate, leading to the desired product (**4a–o**) and the regeneration of the catalyst (Fe_3O_4@CS@Ni_2B) in the reaction mixture. Scheme 3 illustrates the mechanism for synthesizing the desired product, tetrahydrobenzo[*b*]pyran.

2.4 Experiments on the recovery and reusability of the nanocomposite

The recycling and reuse of catalysts are important aspects of industrial processes. If a catalyst can be reused easily and cost-effectively in chemical reactions, it offers significant advantages for industrial applications. This study investigated the recyclability and reusability of Fe_3O_4@CS@Ni_2B in the one-pot synthesis of 2-amino-7,7-dimethyl-5-oxo-4-phenyl-5,6,7,8-tetrahydro-4*H*-chromene-3-carbonitrile, using the reaction of benzaldehyde, dimedone, and malononitrile as a model under optimal conditions. To reuse the catalyst after the reaction, 3 mL of hot ethyl acetate was added to the reaction mixture and heated to dissolve the product. The nanocatalyst was then separated from the reaction mixture using an external magnet and washed with ethanol. After washing, the catalyst was dried

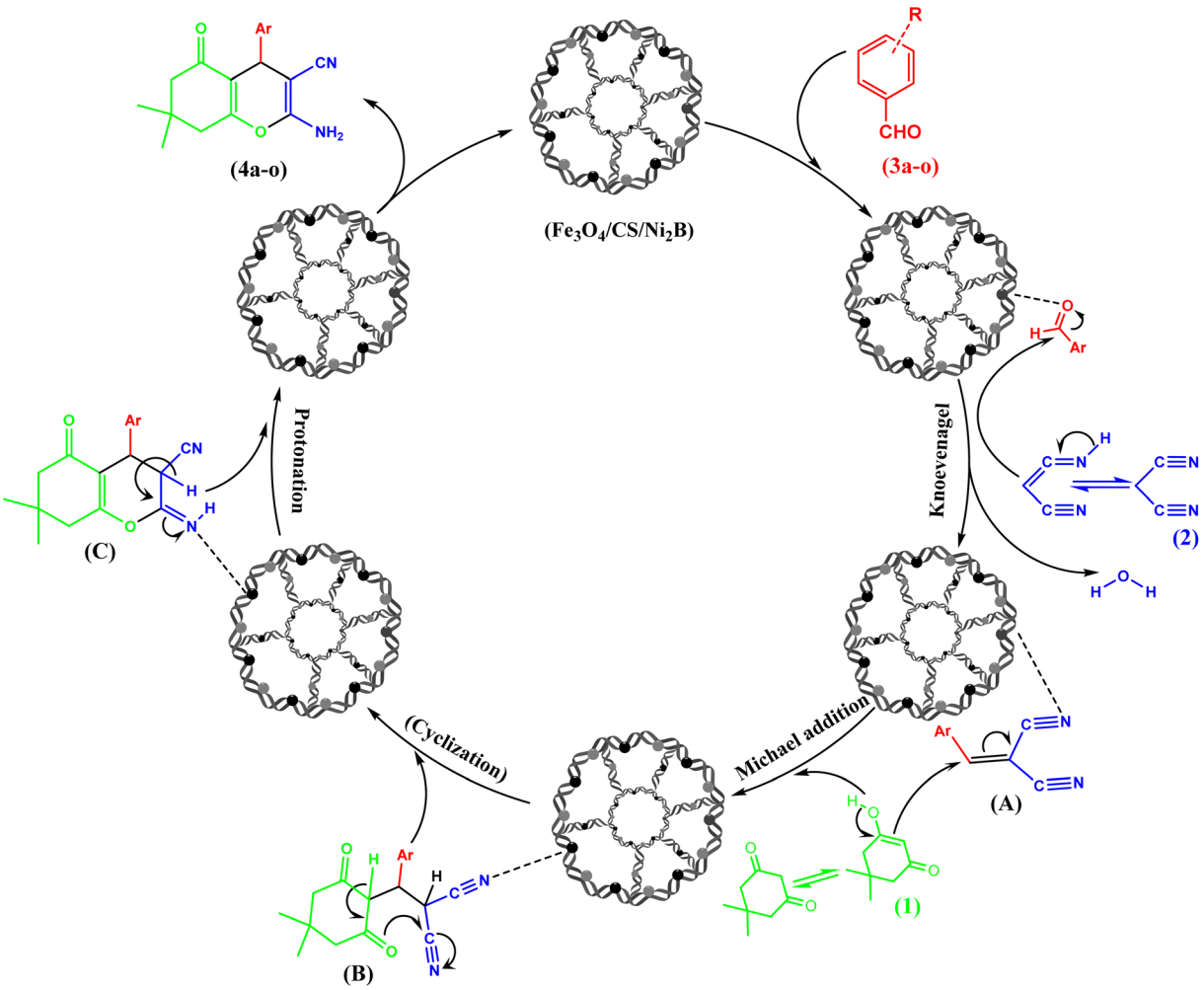

Scheme 3 Plausible mechanism for synthesis of tetrahydrobenzo[*b*]pyran catalyzed by the Fe_3O_4@CS@Ni_2B nanocomposite.

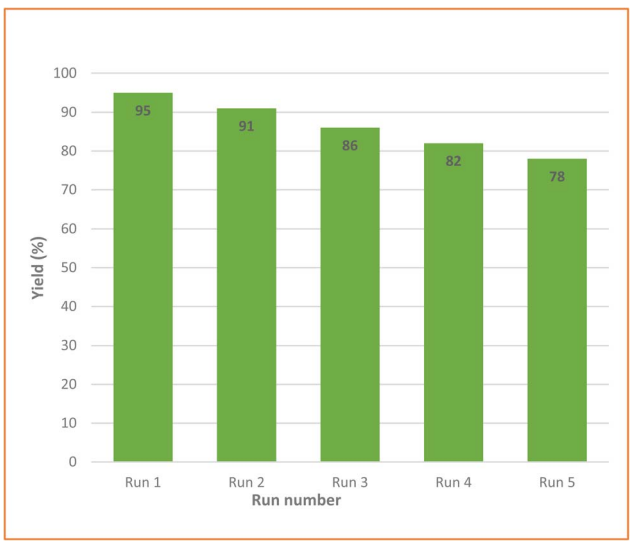

Fig. 12 Reusability diagram of the Fe_3O_4@CS@Ni_2B nanocatalyst.

in an oven and used for the next run. This process was repeated for five runs (Fig. 12). A comparative BET analysis of the Fe_3O_4@CS@Ni_2B catalyst reveals a significant reduction in the surface area from 101.02 $m^2\ g^{-1}$ in the fresh catalyst to 53.125 $m^2\ g^{-1}$ after five catalytic cycles. Despite this decrease, both isotherms exhibit an H3 hysteresis loop, indicating that the fundamental slit-like mesoporous structure remains largely intact (Table 5). In its pristine state, the high surface area of 101.02 $m^2\ g^{-1}$ suggests a well-developed porous network, allowing optimal mass transport and maximal exposure of active sites.

The chitosan matrix, supporting the Fe_3O_4 core and Ni_2B active phase, contributes to this structural integrity. Such characteristics are essential for catalytic efficiency, as they ensure effective reactant adsorption and interaction with active centers. After five reusability cycles, the surface area decreases by approximately 47.5%, likely due to pore blockage from adsorbed byproducts, structural rearrangement, or nanoparticle sintering and aggregation. However, the retention of the H3 hysteresis loop suggests that while overall pore accessibility is reduced, the mesoporous architecture remains functional. This structural persistence implies that active sites,

Table 5 Results of BET analysis for reusability (5 runs) of the nanocomposite[a]

Sample	BET surface area (S_{BET}) ($m^2\ g^{-1}$)	V_m (cm^3(STP) g^{-1})	Pore volume (V_p) ($cm^3\ g^{-1}$)	Pore size (nm)
Primary Fe_3O_4@CS@Ni_2B	101.02	23.21	0.3016	11.94
5 runs – Fe_3O_4@CS@Ni_2B	53.125	12.206	0.2101	15.817

[a] S_{BET}: Brunauer–Emmett–Teller surface area. V_m: Brunauer–Emmett–Teller volume of monolayer coverage. V_p: BJH desorption cumulative volume of pores.

although fewer, are still accessible to reactants, allowing continued catalytic performance. From an industrial perspective, this catalyst's ability to retain its mesoporous morphology despite multiple uses underscores its reusability and operational stability. While some reduction in catalytic efficiency may be expected, the material's structural robustness minimizes the need for frequent replacement, contributing to cost-effective and sustainable catalytic processes. Ultimately, while BET analysis indicates a decline in the accessible surface area, the preserved mesoporosity and continued accessibility of active sites highlight the practical viability of Fe_3O_4@chitosan@Ni_2B as a reusable catalyst (Fig. 13). The Fe_3O_4@CS@Ni_2B catalyst was analyzed through FESEM imaging in two stages (Fig. 14 and 15): after 3 reaction runs and after 5 runs. The comparative evaluation highlights its structural integrity and sustained catalytic performance over multiple reuses.

Initially, the fresh catalyst exhibits well-dispersed, nearly spherical Ni_2B nanoparticles anchored onto a chitosan-coated Fe_3O_4 support. The chitosan matrix is intact, preventing agglomeration and ensuring a high density of active sites, contributing to optimal catalytic efficiency.

After 3 runs, minor morphological modifications emerge. Slight nanoparticle clustering and localized chitosan disruptions are observed, yet the matrix remains largely intact, preserving its structural role. The catalyst retains most of its active surface area, indicating minimal performance loss. By the 5th run, enhanced but controlled sintering occurs, leading to moderate nanoparticle agglomeration. The chitosan framework shows increased irregularities but still stabilizes the active phase. Despite a rougher surface, the essential morphology remains preserved, maintaining a significant portion of reactive sites.

Overall, the FESEM analysis confirms that while the catalyst undergoes gradual morphological evolution, it retains sufficient structural integrity for sustained catalytic activity over multiple runs. The findings underscore its reusability, with only minimal degradation affecting performance.

2.5 A comparative study

The current protocol was thoroughly compared with other reported protocols for the synthesis of 2-amino-4-aryl-7,7-dimethyl-5-oxo-5,6,7,8-tetrahydro-4*H*-chromene-3-carbonitrile using the prepared Fe_3O_4@CS@Ni_2B nanocomposite. The comparison highlights the high efficiency and value of the proposed method, validating its effectiveness under different conditions such as catalyst loading, reaction time, optimal yield, and eco-friendliness compared to previously available procedures (Table 6).

3 Experimental

3.1 Materials and instruments

All reagents and solvents used in the synthesis were obtained from commercial sources and utilized without further purification. The progress of the reaction was monitored using thin-

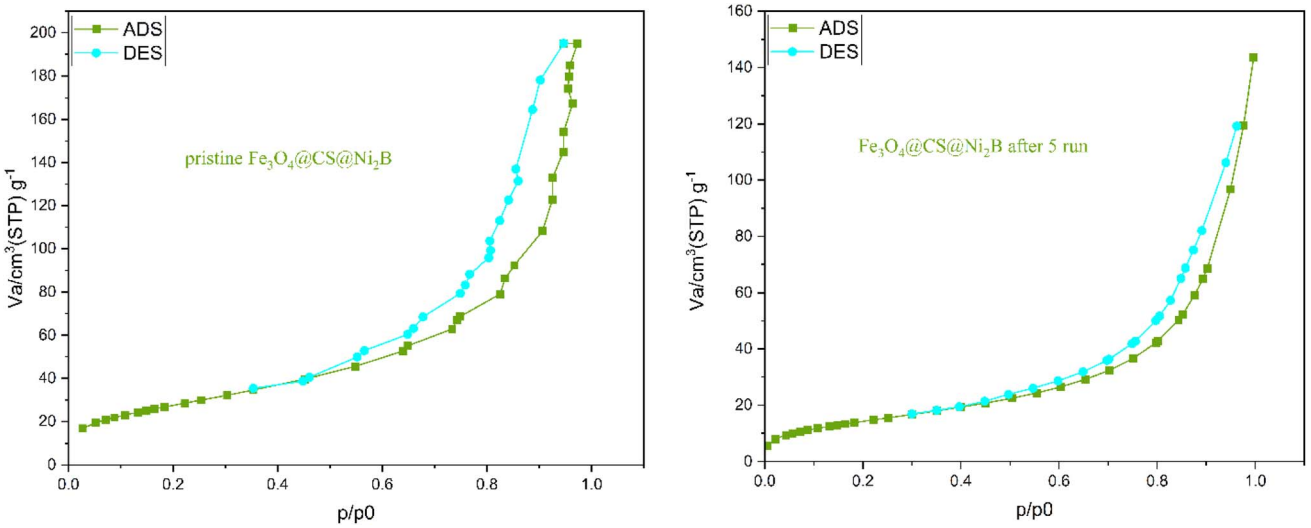

Fig. 13 N_2 adsorption–desorption isotherms of Fe_3O_4@CS@Ni_2B (pristine and after 5 runs).

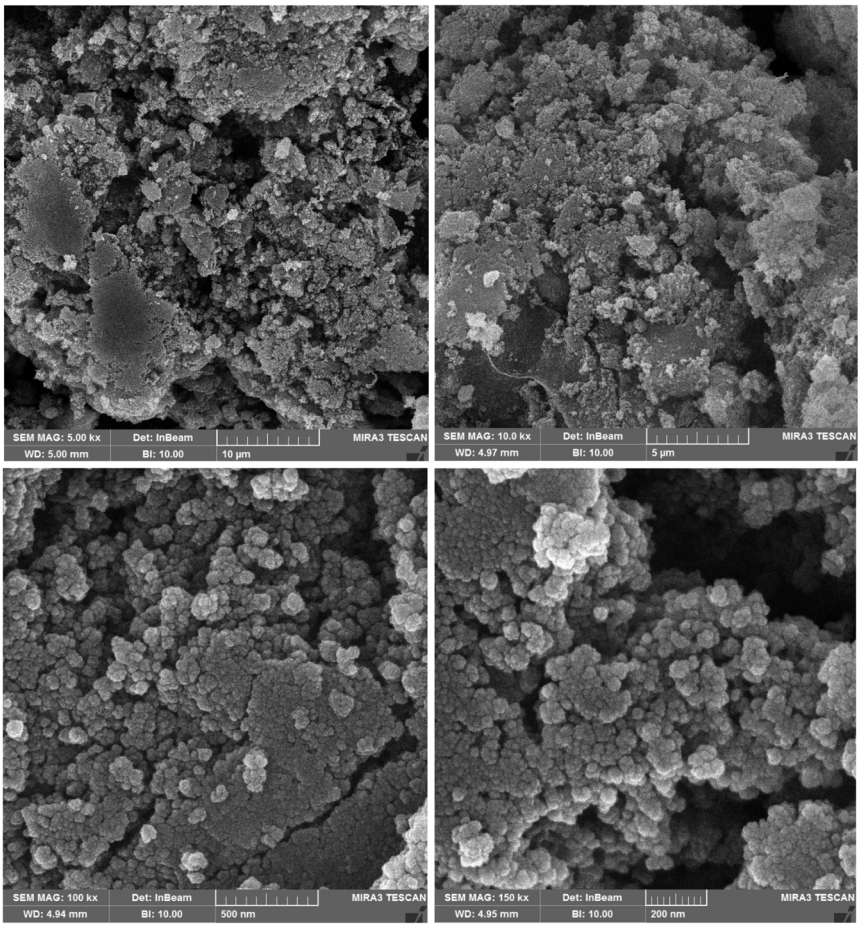

Fig. 14 Reusability FESEM image of the Fe_3O_4@CS@Ni_2B nanocatalyst after 3 runs.

layer chromatography (TLC) with silica gel as the adsorbent. Infrared (IR) spectra were recorded on a Thermo Nicolet Nexus 670 spectrometer in the range of 400–4000 cm^{-1} using the KBr disk method. The crystallographic characteristics of the samples were analyzed by X-ray diffraction (XRD) using a PANalytical X'Pert PRO (PHILIPS PW1730, with Cu Kα radiation: $\lambda =$ 1.54056 Å; 40 kV, 30 mA). Particle morphology and size distribution were determined *via* scanning electron microscopy (SEM) using a FESEM-TESCAN MIRA3 microscope equipped with an EDX attachment (Czech Republic). The BET (Brunauer–Emmett–Teller) surface area, pore volume, and pore diameter of the samples were measured with a BELSORP MINI II instrument (Japan). The magnetic properties of the sample were analyzed using a vibrating sample magnetometer (VSM, Meghnatis Daghigh Kavir Co., Iran). Thermogravimetric (TG) analysis was carried out using a TA Q-600 instrument.

3.2 Preparation of magnetite Fe_3O_4 nanoparticles (MNPs)

The Fe_3O_4 NPs were synthesized based on the method described in the literature[86] with modifications. For this purpose, $FeCl_3 \cdot 6H_2O$ (2.77 g, 10 mmol) was added to 50 mL of deionized water and stirred. Then, a few drops of concentrated HCl were added, and after complete dissolution, $FeCl_2 \cdot 4H_2O$ (1 g, 5 mmol) was added to the solution and stirred under a nitrogen atmosphere at 80 °C for 10 minutes. Afterward, 8 mL of concentrated ammonia (25%) was added rapidly to the solution under vigorous mechanical stirring. The black mixture was stirred for another 1 hour and then cooled to room temperature. The black nanoparticles of Fe_3O_4 were separated using a magnet. The resulting magnetic particles were washed several times with deionized water, followed by a NaCl solution (0.02 M), and dried at 60 °C.

3.3 Preparation of the CS gel

To prepare the CS gel, powdered CS (0.3 g) was first completely dissolved in 100 mL of 2% v/v acetic acid solution and then precipitated with 2.5 M NaOH solution. Next, the resulting gel was filtered and washed with deionized water until the pH of the runoff was around 7.

3.4 Preparation of Fe_3O_4@CS@Ni_2B

In a three-necked round-bottom flask (100 mL), the succulent CS gel from the previous step was added to 50 mL of deionized water and stirred for 30 min, then sonicated for 30 min. After the addition and dissolution of $Ni(OAc)_2 \cdot 4H_2O$ (0.6 g, 2.41 mmol), 0.3 g of Fe_3O_4 nanoparticles was added and sonicated

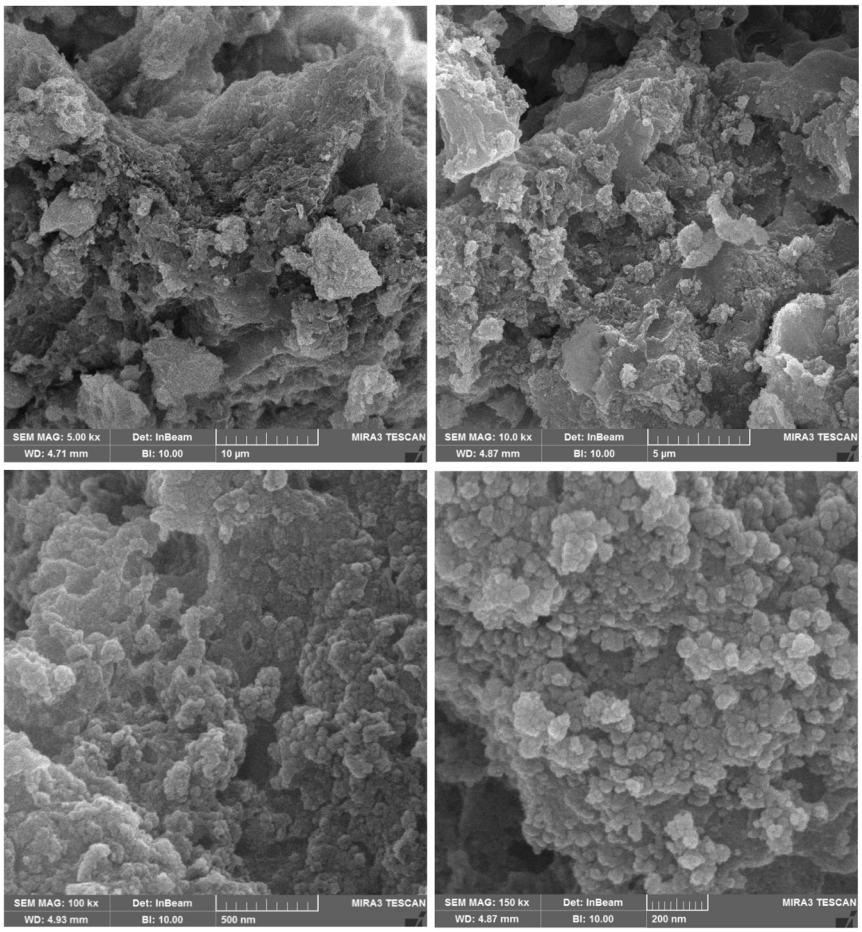

Fig. 15 FESEM image of the Fe_3O_4@CS@Ni_2B nanocomposite after 5 runs.

again for 30 min. The reaction mixture was then degassed under N_2 at 60 °C for 2 hours. Thereafter, the reaction was cooled to room temperature and maintained at 0–5 °C for 30 min in an ice bath with magnetic stirring under a nitrogen atmosphere. A 5 mL portion of a 1.0 M solution of sodium borohydride in 0.1 M sodium hydroxide (NaOH) solution was separately purged with nitrogen and then added to the mixture using a syringe over 30–45 seconds. Immediate formation of a dark precipitate was observed. When gas evolution from the mixture ceased, an additional 2.5 mL of sodium borohydride solution was added dropwise. Next, the ice bath was removed. The precipitates were stirred again at room temperature for 1 hour. The resulting Fe_3O_4@CS@Ni_2B was magnetically separated from the mixture,

Table 6 Comparison of the catalytic activity of the Fe_3O_4@CS@Ni_2B nanocomposite with some reported catalysts for the synthesis of tetrahydrobenzo[*b*]pyran

No.	Catalyst and reaction conditions	Time (min)	Yield (%)	Ref.
1	*p*-Dodecylbenzene sulfonic acid (DBSA)	4 h	90	77
2	AuNPs@RGO-SH	60	85	63
3	ZnO-β zeolite	30	87	78
4	4-(Dimethylamino)pyridine (DMAP)	3 h	76	79
5	Zn_2SnO_4–SnO_2 (25 mg); CH_3CH_2OH; ultrasonic irradiation 80 °C	120	80	80
6	Bis-Su (10 mg); H_2O : CH_3CH_2OH (1 : 1); 80 °C	35	84	81
7	Fe_3O_4@GOQD-*O*-(propane-1-sulfonic acid) (50 mg); H_2O; rt	25	93	82
8	[bmim][BF_4]	4 h	80	83
9	EtOH/reflux/SO_4^{2-}/MCM-41	60	80	65
10	([TEAH]$^+$[OAc]$^-$), 90 °C, solvent free	10	88	84
11	($NiFe_2O_4$@Cu)(H^+ Mont) (20 mg)	50	90	85
12	Fe_3O_4@SiO_2@KCC-1@MPTMS@Cu^{II} (30 mg); solvent-free; 110 °C	60	96	66
13	Fe_3O_4@CS@Ni_2B (20 mg) H_2O : EtOH (1 : 1); reflux	25	95	This work

washed with deionized water and ethanol several times, and dried at 60 °C.

3.5 Preparation of CS/Ni_2B

In a 100 mL three-necked round-bottom flask, the succulent CS gel was added to 50 mL of deoxygenated water and sonicated for 30 min. After the dispersion of CS, the mixture was stirred at 60 °C for 1 hour under a nitrogen atmosphere. $Ni(OAc)_2 \cdot 4H_2O$ (0.6 g, 2.41 mmol) was added and stirred again for 1 hour. After cooling to room temperature, the round-bottom flask was stirred in an ice bath (0–5 °C) under an N_2 atmosphere for 30 minutes. A sodium borohydride solution (5 mL of 1.0 M concentration) in 0.1 M NaOH solution was separately purged with nitrogen and then added quickly to the reaction using a syringe over 30–45 seconds. The color of the solution darkened, and precipitates of CS@Ni_2B formed. When gas evolution from the mixture ceased, 2.5 mL of 1.0 M borohydride solution (in 0.1 M NaOH) was again added dropwise. After this, the ice bath was removed, and the mixture was stirred again at room temperature for 1 hour. Finally, the CS@Ni_2B precipitates were collected by filtration, washed with large amounts of deionized water and ethanol, and then dried at 60 °C.

3.6 General procedure for multicomponent reactions (MCRs) of dimedone with aromatic aldehydes and malononitrile catalyzed by Fe_3O_4@CS@Ni_2B

A mixture of dimedone (1.0 mmol), malononitrile (1.0 mmol), aromatic aldehydes (1.0 mmol), and Fe_3O_4@CS@Ni_2B (20 mg) as a catalyst in 5 mL H_2O : EtOH (1 : 1) as a solvent was stirred at 100 °C for appropriate time. The progress of the reaction was monitored by TLC (eluent: *n*-hexane/EtOAc/MeOH = 8 : 2 : 1). After completion of the reaction, the resulting solid mixture was dissolved in EtOAc followed by magnetic separation of the nanocatalyst. The filtrate was evaporated under reduced pressure, then it was purified by recrystallization from ethanol.

3.7 General procedure for multicomponent reactions (MCRs) of dimedone with aromatic aldehydes and malononitrile catalyzed by CS@Ni_2B

A mixture of dimedone (1.0 mmol), malononitrile (1.0 mmol), aromatic aldehydes (1.0 mmol), and CS@Ni_2B (20 mg) as a catalyst in 5 mL of H_2O : EtOH (1 : 1) as a solvent was stirred at 100 °C for appropriate time. The progress of the reaction was monitored by TLC (eluent: *n*-hexane/EtOAc/MeOH = 8 : 2 : 1). After completion of the reaction, the resulting solid mixture was dissolved in EtOAc, followed by the separation of CS@Ni_2B using filtration. The filtrate was evaporated under reduced pressure, and it was purified by recrystallization from ethanol.

3.8 General procedure for reuse experiments

To reuse the catalyst, 3 mL of hot ethyl acetate was added to the reaction mixture after each run and heated to dissolve the product. The nanocatalyst was then separated from the reaction mixture using an external magnet and washed with ethanol five times to be reused in the next reaction.

4 Conclusion

In conclusion, we present a one-pot three-component condensation process using a novel magnetic nanocatalyst, which was effectively prepared and characterized by FT-IR, XRD, TGA/DTA, BET, FESEM, and VSM studies. The as-prepared Fe_3O_4@CS@Ni_2B magnetic nanocomposite was used as an efficient catalytic system in the synthesis of tetrahydrobenzo[*b*]pyran, a chemical and potentially biologically important derivative, *via* a reaction combining various aldehydes, malononitrile, and dimedone. One of the method's most notable advantages was using water as a solvent and fully green and eco-friendly components throughout the catalyst production process. Furthermore, because all components are inexpensive and readily accessible, the catalyst was produced easily and economically. Another benefit of this procedure was that all target products were prepared in a green manner. Furthermore, the as-prepared nanocomposite demonstrated excellent recyclability as it could be easily recovered from the reaction mixture using an external magnet and reused for five consecutive runs, which is an important benefit in the chemical industry.

Data availability

The data that support the findings of this study are available from the corresponding author upon reasonable request.

Conflicts of interest

There are no conflicts to declare.

Acknowledgements

The authors thank the Research Council of Urmia University for providing financial support to this work.

References

1 D. Çelik and M. Yıldız, Investigation of hydrogen production methods in accordance with green chemistry principles, *Int. J. Hydrogen Energy*, 2017, **42**(36), 23395–23401.
2 X. Ma, *et al.*, Solvent-free Heck reaction catalyzed by a recyclable Pd catalyst supported on SBA-15 via an ionic liquid, *Green Chem.*, 2008, **10**(1), 59–66.
3 P. T. Anastas, M. M. Kirchhoff and T. C. Williamson, Catalysis as a foundational pillar of green chemistry, *Appl. Catal., A*, 2001, **221**(1–2), 3–13.
4 G. Centi and S. Perathoner, Catalysis: role and challenges for a sustainable energy, *Top. Catal.*, 2009, **52**(8), 948–961.
5 M. Rinaudo, Chitin and chitosan: Properties and applications, *Prog. Polym. Sci.*, 2006, **31**(7), 603–632.
6 N. Singh, *et al.*, Chitosan-graphene oxide hydrogels with embedded magnetic iron oxide nanoparticles for dye removal, *ACS Appl. Nano Mater.*, 2019, **2**(11), 7379–7392.
7 A. Rebekah, *et al.*, Magnetic graphene/chitosan nanocomposite: A promising nano-adsorbent for the

removal of 2-naphthol from aqueous solution and their kinetic studies, *Int. J. Biol. Macromol.*, 2020, **159**, 530–538.
8 N. Nuryono, *et al.*, Chitosan-functionalized natural magnetic particle@silica modified with (3-chloropropyl) trimethoxysilane as a highly stable magnetic adsorbent for gold(III) ion, *Mater. Chem. Phys.*, 2020, **255**, 123507.
9 C.-A. Ghiorghita, *et al.*, Porous thiourea-grafted-chitosan hydrogels: Synthesis and sorption of toxic metal ions from contaminated waters, *Colloids Surf., A*, 2020, **607**, 125504.
10 C. Jiang, *et al.*, Adsorption performance of a polysaccharide composite hydrogel based on crosslinked glucan/chitosan for heavy metal ions, *Composites, Part B*, 2019, **169**, 45–54.
11 M. Rajamani and K. Rajendrakumar, Chitosan-boehmite desiccant composite as a promising adsorbent towards heavy metal removal, *J. Environ. Manage.*, 2019, **244**, 257–264.
12 L. Li, *et al.*, Preparation of graphene oxide/chitosan complex and its adsorption properties for heavy metal ions, *Green Process. Synth.*, 2020, **9**(1), 294–303.
13 K. E. Mouaden, *et al.*, Thiocarbohydrazide-crosslinked chitosan as a bioinspired corrosion inhibitor for protection of stainless steel in 3.5% NaCl, *Sustainable Chem. Pharm.*, 2020, **15**, 100213.
14 K. Venkataprasanna, *et al.*, Fabrication of Chitosan/PVA/GO/CuO patch for potential wound healing application, *Int. J. Biol. Macromol.*, 2020, **143**, 744–762.
15 H. Bao, *et al.*, Chitosan-functionalized graphene oxide as a nanocarrier for drug and gene delivery, *Small*, 2011, **7**(11), 1569–1578.
16 H. F. G. Barbosa, *et al.*, Synthesis, characterization and biological activities of biopolymeric schiff bases prepared with chitosan and salicylaldehydes and their Pd(II) and Pt(II) complexes, *Molecules*, 2017, **22**(11), 1987.
17 S. Chen, G. Wu and H. Zeng, Preparation of high antimicrobial activity thiourea chitosan–Ag+ complex, *Carbohydr. Polym.*, 2005, **60**(1), 33–38.
18 S. Ashiri and E. Mehdipour, Preparation of a novel palladium catalytic hydrogel based on graphene oxide/chitosan NPs and cellulose nanowhiskers, *RSC Adv.*, 2018, **8**(57), 32877–32885.
19 X. Cai, *et al.*, Magnetically recyclable core–shell Fe_3O_4@chitosan-Schiff base complexes as efficient catalysts for aerobic oxidation of cyclohexene under mild conditions, *J. Mol. Catal. A: Chem.*, 2014, **383**, 217–224.
20 V. K. Thakur and M. K. Thakur, Recent advances in graft copolymerization and applications of chitosan: a review, *ACS Sustain. Chem. Eng.*, 2014, **2**(12), 2637–2652.
21 G. Cardenas, P. Orlando and T. Edelio, Synthesis and applications of chitosan mercaptanes as heavy metal retention agent, *Int. J. Biol. Macromol.*, 2001, **28**(2), 167–174.
22 R. Ye, *et al.*, Foundations and strategies of the construction of hybrid catalysts for optimized performances, *Nat. Catal.*, 2018, **1**(5), 318–325.
23 H. Mousavi, A comprehensive survey upon diverse and prolific applications of chitosan-based catalytic systems in one-pot multi-component synthesis of heterocyclic rings, *Int. J. Biol. Macromol.*, 2021, **186**, 1003–1166.
24 L. Fan, *et al.*, Fabrication of novel magnetic chitosan grafted with graphene oxide to enhance adsorption properties for methyl blue, *J. Hazard. Mater.*, 2012, **215**, 272–279.
25 M. Nasrollahzadeh, *et al.*, Copper(II) complex anchored on magnetic chitosan functionalized trichlorotriazine: An efficient heterogeneous catalyst for the synthesis of tetrazole derivatives, *Colloid Interface Sci. Commun.*, 2021, **44**, 100471.
26 M. H. Galehban, B. Zeynizadeh and H. Mousavi, Ni^{II} NPs entrapped within a matrix of l-glutamic acid cross-linked chitosan supported on magnetic carboxylic acid-functionalized multi-walled carbon nanotube: a new and efficient multi-task catalytic system for the green one-pot synthesis of diverse heterocyclic frameworks, *RSC Adv.*, 2022, **12**(26), 16454–16478.
27 J. Nagamatsu, *et al.*, Superconductivity at 39 K in magnesium diboride, *Nature*, 2001, **410**(6824), 63–64.
28 H.-Y. Chung, *et al.*, Synthesis of ultra-incompressible superhard rhenium diboride at ambient pressure, *Science*, 2007, **316**(5823), 436–439.
29 B. Albert and H. Hillebrecht, Boron: elementary challenge for experimenters and theoreticians, *Angew. Chem., Int. Ed.*, 2009, **48**(46), 8640–8668.
30 R. Mohammadi, *et al.*, Tungsten tetraboride, an inexpensive superhard material, *Proc. Natl. Acad. Sci. U. S. A.*, 2011, **108**(27), 10958–10962.
31 J. Castaing and P. Costa, Properties and uses of diborides, in *Boron and Refractory Borides*, Springer, 1977, pp. 390–412.
32 M. Neupane, *et al.*, Surface electronic structure of the topological Kondo-insulator candidate correlated electron system SmB_6, *Nat. Commun.*, 2013, **4**(1), 1–7.
33 H. Schlesinger, *et al.*, Sodium borohydride, its hydrolysis and its use as a reducing agent and in the generation of hydrogen1, *J. Am. Chem. Soc.*, 1953, **75**(1), 215–219.
34 C. A. Brown and H. C. Brown, The reaction of sodium borohydride with nickel acetate in aqueous solution - a convenient synthesis of an active nickel hydrogenation catalyst of low isomerizing tendency, *J. Am. Chem. Soc.*, 1963, **85**(7), 1003–1005.
35 H. C. Brown and C. A. Brown, The reaction of sodium borohydride with nickel acetate in ethanol solution - a highly selective nickel hydrogenation catalyst, *J. Am. Chem. Soc.*, 1963, **85**(7), 1005–1006.
36 J. M. Khurana and P. Sharma, Chemoselective reduction of α,β-unsaturated aldehydes, ketones, carboxylic acids, and esters with nickel boride in methanol–water, *Bull. Chem. Soc. Jpn.*, 2004, **77**(3), 549–552.
37 L. An, *et al.*, Nickel iron boride nanosheets on rGO for active electrochemical water oxidation, *J. Solid State Chem.*, 2018, **265**, 135–139.
38 W. Yuan, *et al.*, Performance of surface-oxidized Ni_3B, Ni_2B, and NiB_2 electrocatalysts for overall water splitting, *ChemElectroChem*, 2019, **6**(3), 764–770.
39 X. Cao, *et al.*, Strongly coupled nickel boride/graphene hybrid as a novel electrode material for supercapacitors, *Chem. Eng. J.*, 2017, **327**, 1085–1092.

40 T. D. Çiftçi and E. Henden, Nickel/nickel boride nanoparticles coated resin: A novel adsorbent for arsenic(III) and arsenic(V) removal, *Powder Technol.*, 2015, **269**, 470–480.
41 C. Shu, *et al.*, Desulfurization of diesel fuel with nickel boride in situ generated in an ionic liquid, *Green Chem.*, 2014, **16**(8), 3881–3889.
42 A. Lako, Towards nickel boride catalyzed C–C coupling reactions, KD200X - Master Thesis, KTH Royal Institute of Technology, 2017, **https://kth.diva-portal.org/smash/get/diva2:1150874/FULLTEXT01.pdf**.
43 F. M. Aminzadeh and B. Zeynizadeh, Immobilized nickel boride nanoparticles on magnetic functionalized multi-walled carbon nanotubes: a new nanocomposite for the efficient one-pot synthesis of 1,4-benzodiazepines, *Nanoscale Adv.*, 2023, **5**(17), 4499–4520.
44 J. A. Schreifels, P. C. Maybury and W. E. Swartz Jr, Comparison of the activity and lifetime of Raney nickel and nickel boride in the hydrogenation of various functional groups, *J. Org. Chem.*, 1981, **46**(7), 1263–1269.
45 B. Zeynizadeh, H. Mousavi and F. M. Aminzadeh, A hassle-free and cost-effective transfer hydrogenation strategy for the chemoselective reduction of arylnitriles to primary amines through in situ-generated nickel^{II} dihydride intermediate in water, *J. Mol. Struct.*, 2022, **1255**, 131926.
46 G. Proietti, *et al.*, Nickel boride catalyzed reductions of nitro compounds and azides: nanocellulose-supported catalysts in tandem reactions, *Synthesis*, 2022, **54**(01), 133–146.
47 C. Hulme and V. Gore, Multi-component reactions: emerging chemistry in drug discovery from Xylocain to Crixivan, *Curr. Med. Chem.*, 2003, **10**(1), 51–80.
48 A. Dömling, Recent developments in isocyanide based multicomponent reactions in applied chemistry, *Chem. Rev.*, 2006, **106**(1), 17–89.
49 Y. Gu, Multicomponent reactions in unconventional solvents: state of the art, *Green Chem.*, 2012, **14**(8), 2091–2128.
50 M. Esmati and B. Zeynizadeh, Introducing rGO@Fe_3O_4@Ni as an efficient magnetic nanocatalyst for the synthesis of tetrahydrobenzopyranes via multicomponent coupling reactions of dimedone, malononitrile, and aromatic aldehydes, *Appl. Organomet. Chem.*, 2022, **36**(2), e6496.
51 S. M. Gomha and F. M. Abdelrazek, A facile three-component one-pot synthesis of some novel tricyclic hetero-ring systems, *J. Heterocycl. Chem.*, 2016, **53**(6), 1892–1896.
52 S. Zhaleh, *et al.*, Chitosan: a sustainable, reusable and biodegradable organocatalyst for green synthesis of 1,4-dihydropyridine derivatives under solvent-free condition, *Res. Chem. Intermed.*, 2016, **42**(12), 8069–8081.
53 A. Maleki and R. Paydar, Bionanostructure-catalyzed one-pot three-component synthesis of 3,4-dihydropyrimidin-2(1*H*)-one derivatives under solvent-free conditions, *React. Funct. Polym.*, 2016, **109**, 120–124.
54 J. Safari and L. Javadian, Ultrasound assisted the green synthesis of 2-amino-4*H*-chromene derivatives catalyzed by Fe_3O_4-functionalized nanoparticles with chitosan as a novel and reusable magnetic catalyst, *Ultrason. Sonochem.*, 2015, **22**, 341–348.
55 H. Naeimi and S. Lahouti, Magnetic nanoparticles coated with a chitosan anchored Schiff base complex of nickel(II) as an effective, reusable catalyst for one-pot synthesis of spirolactones, *Transition Met. Chem.*, 2018, **43**(3), 221–229.
56 R. Mohammadi, *et al.*, Chitosan synergistically enhanced by successive Fe_3O_4 and silver nanoparticles as a novel green catalyst in one-pot, three-component synthesis of tetrahydrobenzo[α]xanthene-11-ones, *J. Mol. Catal. A: Chem.*, 2014, **393**, 309–316.
57 A. D. Patil, *et al.*, The inophyllums, novel inhibitors of HIV-1 reverse transcriptase isolated from the Malaysian tree, Calophyllum inophyllum Linn, *J. Med. Chem.*, 1993, **36**(26), 4131–4138.
58 S. A. Patil, *et al.*, Chromenes: potential new chemotherapeutic agents for cancer, *Future Med. Chem.*, 2013, **5**(14), 1647–1660.
59 A. Kulshrestha, *et al.*, Microtubule inhibitor, SP-6-27 inhibits angiogenesis and induces apoptosis in ovarian cancer cells, *Oncotarget*, 2017, **8**(40), 67017.
60 D. Kumar, *et al.*, A facile one-pot green synthesis and antibacterial activity of 2-amino-4*H*-pyrans and 2-amino-5-oxo-5,6,7,8-tetrahydro-4*H*-chromenes, *Eur. J. Med. Chem.*, 2009, **44**(9), 3805–3809.
61 A. Schinkovitz, *et al.*, Ostruthin: an antimycobacterial coumarin from the roots of Peucedanum ostruthium, *Planta Med.*, 2003, **69**(04), 369–371.
62 A.-M. Katsori and D. Hadjipavlou-Litina, Coumarin derivatives: an updated patent review (2012 – 2014), *Expert Opin. Ther. Pat.*, 2014, **24**(12), 1323–1347.
63 H. Naeimi and M. Farahnak Zarabi, Gold nanoparticles supported on thiol-functionalized reduced graphene oxide as effective recyclable catalyst for synthesis of tetrahydro-4*H*-chromenes in aqueous media, *Appl. Organomet. Chem.*, 2018, **32**(4), e4225.
64 D. S. Aher, *et al.*, Quaternary vanado-molybdotungstophosphoric acid [$H_5PW_6Mo_4V_2O_{40}$] over natural montmorillonite as a heterogeneous catalyst for the synthesis 4*H*-pyran and polyhydroquinoline derivatives, *ChemistrySelect*, 2020, **5**(25), 7320–7331.
65 M. Abdollahi-Alibeik and F. Nezampour, Synthesis of 4*H*-benzo[*b*]pyrans in the presence of sulfated MCM-41 nanoparticles as efficient and reusable solid acid catalyst, *React. Kinet., Mech. Catal.*, 2013, **108**, 213–229.
66 M. H. Galehban, B. Zeynizadeh and H. Mousavi, Diverse and efficient catalytic applications of new cockscomb flower-like Fe_3O_4@SiO_2@KCC-1@MPTMS@Cu^{II} mesoporous nanocomposite in the environmentally benign reduction and reductive acetylation of nitroarenes and one-pot synthesis of some coumarin compounds, *RSC Adv.*, 2022, **12**(18), 11164–11189.
67 S. Gharghish, M. G. Dekamin and S. H. Banakar, Functionalized graphene oxide by 4-amino-3-hydroxy-1-naphthalenesulfonic acid as a heterogeneous nanocatalyst for the one-pot synthesis of tetraketone and

tetrahydrobenzo[*b*]pyran derivatives under green conditions, *Nanoscale Adv.*, 2024, **6**(15), 3911–3922.

68 F. Ataie, A. Davoodnia and A. Khojastehnezhad, Graphene oxide functionalized organic-inorganic hybrid (GO–Si–NH_2–PMo): An efficient and green catalyst for the synthesis of tetrahydrobenzo[*b*]pyran derivatives, *Polycyclic Aromat. Compd.*, 2021, **41**(4), 781–794.

69 S. Sadjadi, *et al.*, Halloysite nanoclay with high content of sulfonic acid-based ionic liquid: a novel catalyst for the synthesis of tetrahydrobenzo[*b*]pyrans, *Catalysts*, 2021, **11**(10), 1172.

70 D. Mallah, B. B. F. Mirjalili and A. Bamoniri, Fe_3O_4@nano-almondshell/Si$(CH_2)_3$/2-(1-piperazinyl)ethylamine as an effective magnetite almond shell-based nanocatalyst for the synthesis of dihydropyrano[3,2-*c*]chromene and tetrahydrobenzo[*b*]pyran derivatives, *Sci. Rep.*, 2023, **13**(1), 6376.

71 M. Bakherad, *et al.*, Practical and efficient synthesis of tetrahydrobenzo[*b*]pyran using caffeine supported on silica as an ionic liquid solid acid catalyst, *J. Iran. Chem. Soc.*, 2018, **15**, 2811–2819.

72 M. Bayzidi and B. Zeynizadeh, The immobilized zirconocene chloride on magnetite-reduced graphene ooxide: a highly efficient and reusable heterogeneous nanocatalyst for one-pot three-component synthesis of tetrahydrobenzo[*b*] pyrans and dihydropyrano[3,2-*c*]chromenes, *ChemistrySelect*, 2022, **7**(43), e202202708.

73 Y. Jiang, *et al.*, Facile cross-link method to synthesize magnetic Fe_3O_4@SiO_2–chitosan with high adsorption capacity toward hexavalent chromium, *J. Chem. Eng. Data*, 2018, **64**(1), 226–233.

74 A. L. Bukzem, *et al.*, Optimization of carboxymethyl chitosan synthesis using response surface methodology and desirability function, *Int. J. Biol. Macromol.*, 2016, **85**, 615–624.

75 E. Igberase, A. Ofomaja and P. Osifo, Enhanced heavy metal ions adsorption by 4-aminobenzoic acid grafted on chitosan/epichlorohydrin composite: kinetics, isotherms, thermodynamics and desorption studies, *Int. J. Biol. Macromol.*, 2019, **123**, 664–676.

76 F. Wu, *et al.*, Preparation of an Active Ni_2B/SBA-15 Catalyst to Improve $NaBH_4$ Hydrolysis for Hydrogen Generation, *J. New Mater. Electrochem. Syst.*, 2015, **18**(4), 231–235.

77 E. Sheikhhosseini, D. Ghazanfari and V. Nezamabadi, A new method for synthesis of tetrahydrobenzo[*b*]pyrans and dihydropyrano[*c*]chromenes using *p*-dodecylbenzenesulfonic acid as catalyst in water, *Iran. J. Catal.*, 2013, **3**(4), 197–201.

78 S. S. Katkar, *et al.*, A recyclable and highly effective ZnO-β zeolite as a catalyst for one-pot three-component synthesis of tetrahydrobenzo[*b*]pyrans, *Chin. J. Chem.*, 2011, **29**(1), 199–202.

79 A. T. Khan, *et al.*, One-pot three-component reaction for the synthesis of pyran annulated heterocyclic compounds using DMAP as a catalyst, *Tetrahedron Lett.*, 2011, **52**(41), 5327–5332.

80 M. Ziyaadini, *et al.*, Zn_2SnO_4-SnO_2 nano-composite promoted ultrasonic-assisted synthesis of pyran derivatives, *Polycyclic Aromat. Compd.*, 2022, **42**(2), 460–474.

81 F. Hassanzadeh, *et al.*, Introduction of a new bis-derivative of succinimide (Bis-Su) as a sustainable and efficient basic organo-catalyst for the synthesis of arylidene malononitrile and tetrahydrobenzo[*b*]pyran derivatives under green conditions, *Res. Chem. Intermed.*, 2020, **46**, 4971–4984.

82 M. Khaleghi Abbasabadi, D. Azarifar and H. R. Esmaili Zand, Sulfonic acid-functionalized Fe_3O_4-supported magnetized graphene oxide quantum dots: A novel organic-inorganic nanocomposite as an efficient and recyclable nanocatalyst for the synthesis of dihydropyrano[2,3-*c*]pyrazole and 4*H*-chromene derivatives, *Appl. Organomet. Chem.*, 2020, **34**(12), e6004.

83 X. Fan, *et al.*, Ionic liquid promoted Knoevenagel and Michael reactions, *Aust. J. Chem.*, 2004, **57**(11), 1067–1071.

84 A. Khazaei, *et al.*, Three-component condensation reaction of various aldehydes, dimedone and malononitrile catalyzed by boric acid in water in comparison with multifunctional ionic liquids as green catalytic systems, *Z. Naturforsch., B:J. Chem. Sci.*, 2018, **73**(10), 707–712.

85 B. Zeynizadeh and S. Rahmani, Immobilized copper-layered nickel ferrite on acid-activated montmorillonite,[($NiFe_2O_4$@Cu)(H^+-Mont)], as a superior magnetic nanocatalyst for the green synthesis of xanthene derivatives, *RSC Adv.*, 2019, **9**(48), 28038–28052.

86 S. Karami and B. Zeynizadeh, Reduction of 4-nitrophenol by a disused adsorbent: EDA-functionalized magnetic cellulose nanocomposite after the removal of Cu^{2+}, *Carbohydr. Polym.*, 2019, **211**, 298–307.